Autoinhibition and regulation by phosphoinositides of ATP8B1, a human lipid flippase associated with intrahepatic cholestatic disorders

Thibaud Dieudonné[a,c], Sara Abad Herrera[b#], Michelle Juknaviciute Laursen[c#], Maylis Lejeune[a,1], Charlott Stock[c], Kahina Slimani[a], Christine Jaxel[a], Joseph A. Lyons[d], Cédric Montigny[a], Thomas Günther Pomorski[b,e*], Poul Nissen[c*] and Guillaume Lenoir[a*]

[a] Université Paris-Saclay, CEA, CNRS, Institute for Integrative Biology of the Cell (I2BC), 91198, Gif-sur-Yvette, France

[b] Faculty of Chemistry and Biochemistry, Department of Molecular Biochemistry, Ruhr University Bochum, 44870, Bochum, Germany

[c] DANDRITE, Nordic EMBL Partnership for Molecular Medicine, Department of Molecular Biology and Genetics, Aarhus University, Aarhus, Denmark

[d] Department of Molecular Biology and Genetics, Aarhus University, Aarhus, Denmark

[e] Department of Plant and Environmental Sciences, University of Copenhagen, Frederiksberg, Denmark

[1] Current address: Institut Pasteur, Université de Paris, CNRS UMR3528, Structural Bioinformatics Unit, F-75015 Paris, France

[#] These authors contributed equally to this work

* Corresponding author; E-mail: thomas.guenther-pomorski@ruhr-uni-bochum.de

* Corresponding author; E-mail: pn@mbg.au.dk

* Corresponding author; E-mail: guillaume.lenoir@i2bc.paris-saclay.fr

Running title: Regulatory mechanism of the human flippase ATP8B1

Abstract

P4-ATPases flip lipids from the exoplasmic to the cytosolic leaflet, thus maintaining lipid asymmetry in eukaryotic cell membranes. Mutations in several human P4-ATPase genes are associated with severe diseases, e.g. in *ATP8B1* causing progressive familial intrahepatic cholestasis, a rare inherited disorder progressing toward liver failure. ATP8B1 forms a binary complex with CDC50A and displays a broad specificity to glycerophospholipids, but regulatory mechanisms are unknown. Here, we report functional studies and the cryo-EM structure of the human lipid flippase ATP8B1-CDC50A at 3.1 Å resolution. We find that ATP8B1 is autoinhibited by its N- and C-terminal tails, which form extensive interactions with the catalytic sites and flexible domain interfaces. Consistently, ATP hydrolysis is unleashed by truncation of the C-terminus, but also requires phosphoinositides, most markedly phosphatidylinositol-3,4,5-phosphate (PI(3,4,5)P_3), and removal of both N- and C-termini results in full activation. Restored inhibition of ATP8B1 truncation constructs with a synthetic peptide mimicking the C-terminal segment further suggests molecular communication between N- and C-termini in the autoinhibition and demonstrates that the regulatory mechanism can be interfered with by exogenous compounds. A recurring (G/A)(Y/F)AFS motif of the C-terminal segment suggests that this mechanism is employed widely across P4-ATPase lipid flippases in plasma membrane and endomembranes.

Keywords: Flippases/Autoinhibition/Phosphoinositides/P4-ATPases/Progressive familial intrahepatic cholestasis/Cryo-EM

53 **Introduction**

54

55 Transbilayer lipid asymmetry is a fundamental characteristic of eukaryotic cell and organelle
56 membranes (Kobayashi and Menon, 2018; van Meer, 2011; van Meer et al., 2008; Verkleij et al.,
57 1973). In most cell types choline-containing phosphatidylcholine (PC) and sphingomyelin (SM) are
58 chiefly located in the exoplasmic leaflet while the aminophospholipids phosphatidylserine (PS) and
59 phosphatidylethanolamine (PE), as well as phosphoinositides (PPIns), mostly occupy the
60 cytoplasmic leaflet (Bretscher, 1972; Murate et al., 2015). Phospholipid asymmetry plays an
61 important role in eukaryotic cell function. A well-studied example is the asymmetric distribution of PS
62 in membranes of the late secretory/endocytic pathways, where it confers a high surface charge to
63 these membranes, thereby facilitating the recruitment of polybasic motif-containing protein effectors
64 such as the small G proteins K-Ras (Hancock et al., 1990; Yeung et al., 2009), Cdc42 and ROP6,
65 as well as other proteins like protein kinase C (PKC), synaptotagmin, and the membrane fission
66 protein EHD1 (Bohdanowicz and Grinstein, 2013; Lee et al., 2015; Lemmon, 2008; Leventis and
67 Grinstein, 2010; Platre et al., 2019). Thus, there is a direct link between PS sidedness and regulation
68 of cell polarity, cell signaling and vesicular trafficking. Phospholipid asymmetry is maintained by
69 flippases and floppases, which use ATP for inward and outward movement of lipids across
70 membranes, respectively (Andersen et al., 2016; López-Marqués et al., 2015; Montigny et al., 2016).
71 In contrast, scramblases comprise a third category that passively equilibrates lipids across the
72 bilayer, often controlled by gating (Pomorski and Menon, 2016). Whereas floppases belong to the
73 superfamily of ATP-binding cassette (ABC) transporters, most flippases characterized thus far are
74 from the type 4 subfamily of P-type ATPases, hereafter referred to as P4-ATPases. The human
75 genome encodes 14 P4-ATPases. Using NBD-lipids as fluorescent derivatives of native lipids,
76 ATP8A1, ATP8A2, ATP11A, ATP11B and ATP11C were shown to transport the aminophospholipids
77 NBD-PS and NBD-PE, both in cell-based assays and upon reconstitution in proteoliposomes
78 (Coleman et al., 2009; Lee et al., 2015; Segawa et al., 2016; Wang et al., 2018). By contrast,
79 ATP8B1, ATP8B2 and ATP10A were shown to transport NBD-PC (Naito et al., 2015; Takatsu et al.,
80 2014) and ATP10A and ATP10D catalyze the transport of NBD-glucosylceramide (Roland et al.,
81 2019). Mutations in ATP8A2 and ATP11A have been reported to cause severe neurological
82 disorders (Onat et al., 2013; Segawa et al., 2021), and mutations in ATP8B1 are associated with
83 intrahepatic cholestatic disorders, such as benign recurrent intrahepatic cholestasis (BRIC1),
84 intrahepatic cholestasis of pregnancy (ICP1), and the more severe progressive familial intrahepatic
85 cholestasis type 1 (PFIC1). PFIC1 is a rare inherited liver disorder characterized by impaired bile
86 flow, fat malabsorption and progressive cirrhosis and fibrosis (Jacquemin, 2012; van der Mark et al.,
87 2013).

Similar to many ion-transporting P-type ATPases, P4-ATPases consist of a transmembrane domain containing ten membrane-spanning α-helical segments, as well as three cytosolic domains, the actuator (A), nucleotide-binding (N), and phosphorylation (P) domains involved in catalysis (***Figure 1A***). Importantly, most P4-ATPases form obligatory binary complexes with members of the CDC50 protein family, which are essential for correct targeting of the flippase complex to its final destination and for its transport activity (Coleman and Molday, 2011; Lenoir et al., 2009; Poulsen et al., 2008; Saito et al., 2004; Segawa et al., 2018). Conformational changes in the membrane domain, required to facilitate lipid transport, are coupled to phosphorylation and dephosphorylation events in the cytosolic ATPase domains, thereby allowing efficient lipid transport against concentration gradients. The different steps of the transport cycle are collectively described as the Post-Albers scheme (Albers, 1967; Post et al., 1972), where the P-type ATPase cycles between different conformations, E1, E1P, E2P and E2 (P for phosphorylated) (***Figure 1B***). The transport substrate, a lipid for P4-ATPases, is recognized in the E2P conformation, and its binding triggers dephosphorylation leading to E2 and eventually release of the lipid in the opposing leaflet. The subcellular localization, heteromeric interactions with CDC50 proteins and lipid transport activity of ATP8B1 have been thoroughly investigated using cell-based assays (Bryde et al., 2010; Takatsu et al., 2014; van der Velden et al., 2010). In contrast, ATP8B1 remains poorly studied at the molecular mechanistic level. In particular, while several other P4-ATPases, and P-type ATPases in general, are tightly regulated by lipid co-factors, protein partners, or by their terminal extensions (Azouaoui et al., 2017; Chalat et al., 2017; Holemans et al., 2015; Saffioti et al., 2021; Tsai et al., 2013), the way ATP8B1 activity is regulated remains unknown. Recent high-resolution structures of the yeast Drs2-Cdc50, Dnf1,2-Lem3 and the human ATP8A1-CDC50A and ATP11C-CDC50A flippase complexes have illuminated the molecular mechanism of lipid transport, providing a framework for understanding how these transporters are able to move lipids (Bai et al., 2019, 2020; Hiraizumi et al., 2019; Lyons et al., 2020; Nakanishi et al., 2020b; Timcenko et al., 2019, 2021). A key finding from these high-resolution structures is C-terminal autoinhibition of yeast Drs2 and human ATP8A1 (Hiraizumi et al., 2019; Timcenko et al., 2019). Furthermore, structures of Drs2-Cdc50 obtained in the presence of phosphatidylinositol-4-phosphate (PI(4)P) shed light on the specific regulation of Drs2 by this phosphoinositide, as previously observed using purified enzyme and activity assays (Azouaoui et al., 2017; Natarajan et al., 2009; Zhou et al., 2013).

In this report, we purified human ATP8B1-CDC50A complex, amenable for detailed study of its three-dimensional structure and catalytic activity. We determined the high-resolution structure of an autoinhibited state by cryo-electron microscopy (cryo-EM). In keeping with an observed, tight interaction of the C-terminal tail of ATP8B1 with the cytosolic domains, the ATP8B1-CDC50A complex displayed ATPase activity only after removal of its C-terminus. Using protease cleavage

123 sites within the N-terminus or, for the C-terminus, immediately after the last transmembrane segment
124 of ATP8B1, we demonstrate that ATP8B1 is primarily autoinhibited by its C-terminal extension, but
125 that the N-terminal extension is involved in a synergistic manner. In addition to the importance of
126 these autoregulatory elements, we show that PPIns are critical activators of ATP8B1 activity.

127 **Results**

128

129 **Cryo-EM structure of the ATP8B1-CDC50A complex in the autoinhibited E2P state**

130 Recent studies revealed that flippases can be autoregulated by their C-terminal extensions. In
131 particular, (G/A)(Y/F)AFS motifs in the C-termini of Drs2 and ATP8A1 occupy the nucleotide binding
132 site, thereby preventing conformational changes required for lipid transport (Hiraizumi et al., 2019;
133 Timcenko et al., 2019). This motif is also present in ATP8B1 as ^{1208}AYAF^{1212}S (***Figure 1A***), hinting
134 at a regulatory role of the ATP8B1 C-terminus. To gain insight into the mechanism of ATP8B1
135 regulation, we devised a procedure for co-overexpression of ATP8B1 and CDC50A in
136 *Saccharomyces cerevisiae* and purification of the complex (***Figure 1–figure supplement 1A and***
137 ***1B***). ATP8B1 and CDC50A co-expressed well in yeast and were solubilized from yeast membranes
138 using n-Dodecyl-β-D-Maltoside (DDM) supplemented with cholesteryl hemisuccinate (CHS).
139 Following streptavidin-based affinity chromatography and on-column cleavage of the biotin acceptor
140 domain (BAD) tag with TEV protease, we obtained a highly pure ATP8B1-CDC50A complex (***Figure***
141 ***1C, Figure 1–figure supplement 1C***). Treatment of the purified ATP8B1-CDC50A complex with
142 Endoglycosidase H resulted in consolidation of multiple bands into a single band around 40 kDa, the
143 expected molecular weight of histidine-tagged CDC50A, reflecting various glycosylation levels of its
144 polypeptide chain (***Figure 1–figure supplement 1C***). The stoichiometry between ATP8B1 and
145 CDC50A was found to be 1:1, as determined by in-gel fluorescence (***Figure 1–figure supplement***
146 ***1D and 1E***). P-type ATPases couple autophosphorylation from ATP and subsequent
147 dephosphorylation of a catalytic aspartate in the P-domain to structural changes in the membrane
148 domain, thus transporting substrates across the membrane against steep concentration gradients
149 (***Figure 1B***). To ascertain functionality of the purified complex, we investigated its ability to undergo
150 phosphorylation from [γ-^{32}P]ATP on its catalytic aspartate. The results confirm that the
151 phosphoenzyme involves formation of an aspartyl-phosphate bond on residue D454 (***Figure 1D***).
152 For structural studies, DDM was exchanged for lauryl maltose neopentyl glycol (LMNG). The
153 resulting sample showed a high degree of monodispersity on size-exclusion chromatography
154 (***Figure 1E***).

155

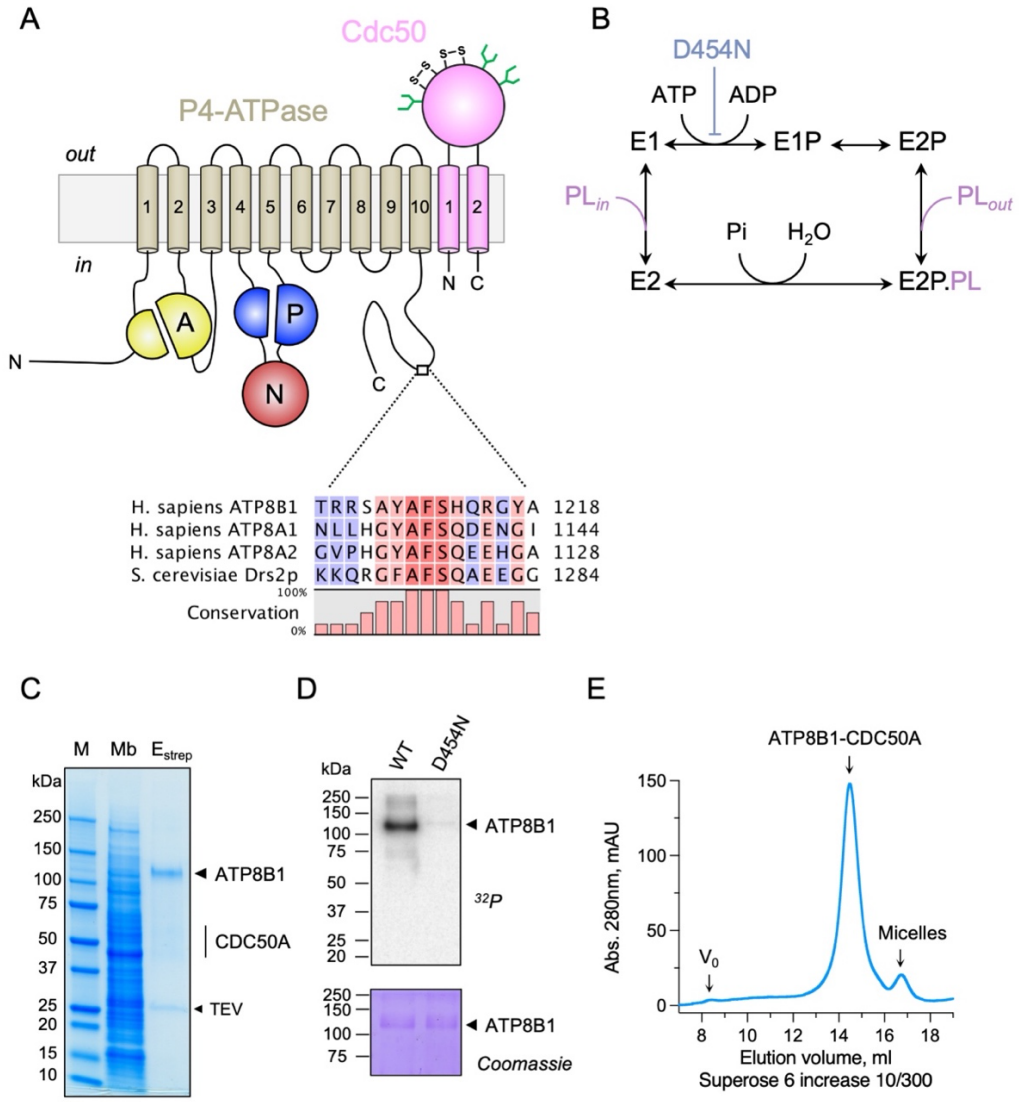

Figure 1 – Purification and functional assessment of the ATP8B1-CDC50A complex expressed in *Saccharomyces cerevisiae*.

(A) Predicted topology of ATP8B1-CDC50A with the transmembrane domain of ATP8B1 in tan and the Actuator domain (A), the Nucleotide binding domain (N) and the Phosphorylation domain (P) in yellow, red, and blue, respectively. CDC50A with two transmembrane spans and a large exoplasmic loop in pink; predicted disulfide bridges (S-S) and glycosylation sites (green) are indicated. Sequence alignment of part of the C-terminus of ATP8B1, ATP8A1, ATP8A2, and Drs2 (CLC Main Workbench, Qiagen). The shading indicates conservation (blue 0% – red 100%). Uniprot accession numbers are P39524 for Drs2, Q9Y2Q0 for ATP8A1, Q9NTI2 for ATP8A2 and O43520 for ATP8B1. *(B)* Post-Albers cycle for P4-ATPases. ATP8B1 mutation D454N prevents phosphorylation on the catalytic aspartate and thus blocks activity. Pi, inorganic phosphate; PL, phospholipid. *(C)* SDS-PAGE analysis of ATP8B1-CDC50A affinity purification on streptavidin beads. Crude yeast membranes (Mb), containing 25 μg of total proteins, of which ATP8B1 represents 0.5%, and ~ 1-1.5 μg proteins recovered upon TEV protease cleavage on streptavidin beads (E_{strep}) were loaded on the gel and visualized by Coomassie Blue staining. M, molecular weight marker. *(D)* Phosphoenzyme formation from [γ-^{32}P]ATP of wild-type and catalytically-inactive D454N variant, as analyzed after electrophoretic separation on acidic gels. Coomassie Blue staining of the same gel was used to control the amount of wild-type and D454N subjected to ^{32}P labeling. *(E)* Size-exclusion chromatography elution profile of the purified human ATP8B1-CDC50A complex used for cryo-EM studies. Arrows indicate the void volume of the column (V_0), as well as the elution volume of the ATP8B1-CDC50A complex and detergent micelles.

176

177 The structure of the full-length complex was then determined using single particle cryo-EM (***Figure***
178 ***2–figure supplement 1***). To stabilize the complex in the autoinhibited E2P conformation
179 ($E2P_{autoinhibited}$), the sample was incubated in the presence of beryllium fluoride (forming e.g. BeF_3^-,
180 $BeF_2(OH_2)$ adducts, referred to as BeF_x) mimicking phosphorylation. The high-resolution map
181 (overall resolution: 3.1Å) obtained by cryo-EM enabled us to model most of ATP8B1 and CDC50A
182 sequences (***Table 1***), except flexible loops and termini.
183

Data collection and processing	
Magnification	130,000x
Voltage (kV)	300
Microscope	Titan Krios (Aarhus University)
Camera	Gatan K3
Physical pixel size (Å/pix)	0.66
Electron exposure (e–/Å^2)	60
Defocus range (µm)	0.7-1.8
Number of movies	3918
Initial particle images (no.)	470,103
Final particle images (no.)	104,643
Symmetry imposed	C1
Map resolution (Å)	3.1
FSC threshold	0.143
Map resolution range (Å)	2.7-4.5
Refinement	
Initial model used (PDB code)	ATP8B1: I-TASSER homology model based on 6ROH CDC50A : 6K7L
Model resolution (Å)	3.3
FSC threshold	0.5
Map sharpening *B* factor (Å^2)	-84
Model composition	
Non-hydrogen atoms	11868
Protein residues	1439
Ligands	1 MG, 1 BEF, 4 Y01, 4 NAG, 1 BMA
B factors (Å^2, min/max/mean)	
Protein	33.89/136.87/67.09
Ligand	41.58/110.52/60.89
R.m.s. deviations	
Bond lengths (Å)	0.002
Bond angles (°)	0.492
Validation	
MolProbity score	1.43
Clashscore	4.74
Poor rotamers (%)	0.08

Ramachandran plot	
Favored (%)	96.92
Allowed (%)	3.08
Disallowed (%)	0.0

Table 1: Cryo-EM data collection, refinement, and validation statistics

As expected, ATP8B1 harbors a typical P4-ATPase fold with a transmembrane helical bundle made of 10 α-helical segments, a nucleotide binding domain (N), a phosphorylation domain (P) and an actuator domain (A). Comparison with other P4-ATPase structures and the presence of an extra density in the phosphorylation site confirmed that our structure resembles an $E2P_{autoinhibited}$ state with bound BeF_x (***Figure 2–figure supplement 2***). Both CDC50A and CDC50B have been found to interact with ATP8B1 and to promote its trafficking to the plasma membrane (Bryde et al., 2010). As observed for other P4-ATPase/Cdc50 complexes (Bai et al., 2019; Hiraizumi et al., 2019; Nakanishi et al., 2020b; Timcenko et al., 2019), CDC50A interacts extensively with ATP8B1, through its extracellular, transmembrane, and N-terminal region. The extracellular domain of CDC50A covers all the extracellular loops of ATP8B1 except the TM1-2 loop while the N-terminal tail extends parallel to the membrane, interacting with TM6-7 and TM8-9 loops of ATP8B1, as well as with the segment linking TM4 to the P-domain, as previously described (Hiraizumi et al., 2019; Timcenko et al., 2019). The transmembrane domain of CDC50A is made of two interacting transmembrane α-helices and three *N*-linked glycosylation sites are clearly visible in the cryo-EM map (N107, N180, and N294), indicating that *S. cerevisiae* supports glycosylation of this human transporter. CDC50A exhibited a structure nearly identical to that observed in the ATP8A1-CDC50A and ATP11C-CDC50A human complexes (Hiraizumi et al., 2019; Nakanishi et al., 2020a), with a RSMD of 0.8 and 1.1 Å respectively (***Figure 2–figure supplement 3***).

In addition, the cryo-EM data displayed very clear densities for parts of the N- and C-termini of ATP8B1 (***Figure 3A, Figure 3–figure supplement 1***). Interestingly, the N-terminal region (Q16-D27) was found to interact tightly with the P-, A- and the N-domain of ATP8B1 (***Figure 3B***). Regarding the interaction of the N-terminal tail with the P-domain, residues D26 and D27 are involved in electrostatic interactions with side chains of N807 and T869, respectively. The interaction is further enhanced by hydrophobic interactions between P17 and W805. The N-terminal tail interacts with the A-domain through hydrogen bonds between S25 and R271 and is further reinforced by hydrophobic interaction between Y24 and L272. Finally, the interaction of the N-terminal tail with the N-domain is mediated by a hydrogen bond between E20 and S598 (***Figure 3B***). Similarly, the C-terminal tail of ATP8B1 engages in hydrogen bonds as well as several salt bridges and hydrophobic interactions with the three cytosolic domains (***Figure 3C***). Noteworthily, F1211 in the conserved AYAFS motif interacts via π-π interactions with F596 in the N-domain, which normally

217 interacts with the adenosine ring of ATP in P-type ATPases, thereby preventing ATP binding.
218 Hydrogen bonds between T1204-Q640, R1206-A647, S1207-D622, and S1212-S552 pairs further
219 promote tight interaction between the C-ter tail and the N-domain. Interactions of the C-terminal tail
220 with the A- and P-domains are mediated by salt bridges (between R1228 and E219 and between
221 R1194 and E751) or via hydrogen bonding between the side chains of Y1217 and R1193 with the
222 backbone carbonyl groups of L237 and A745, respectively (***Figure 3C***).
223

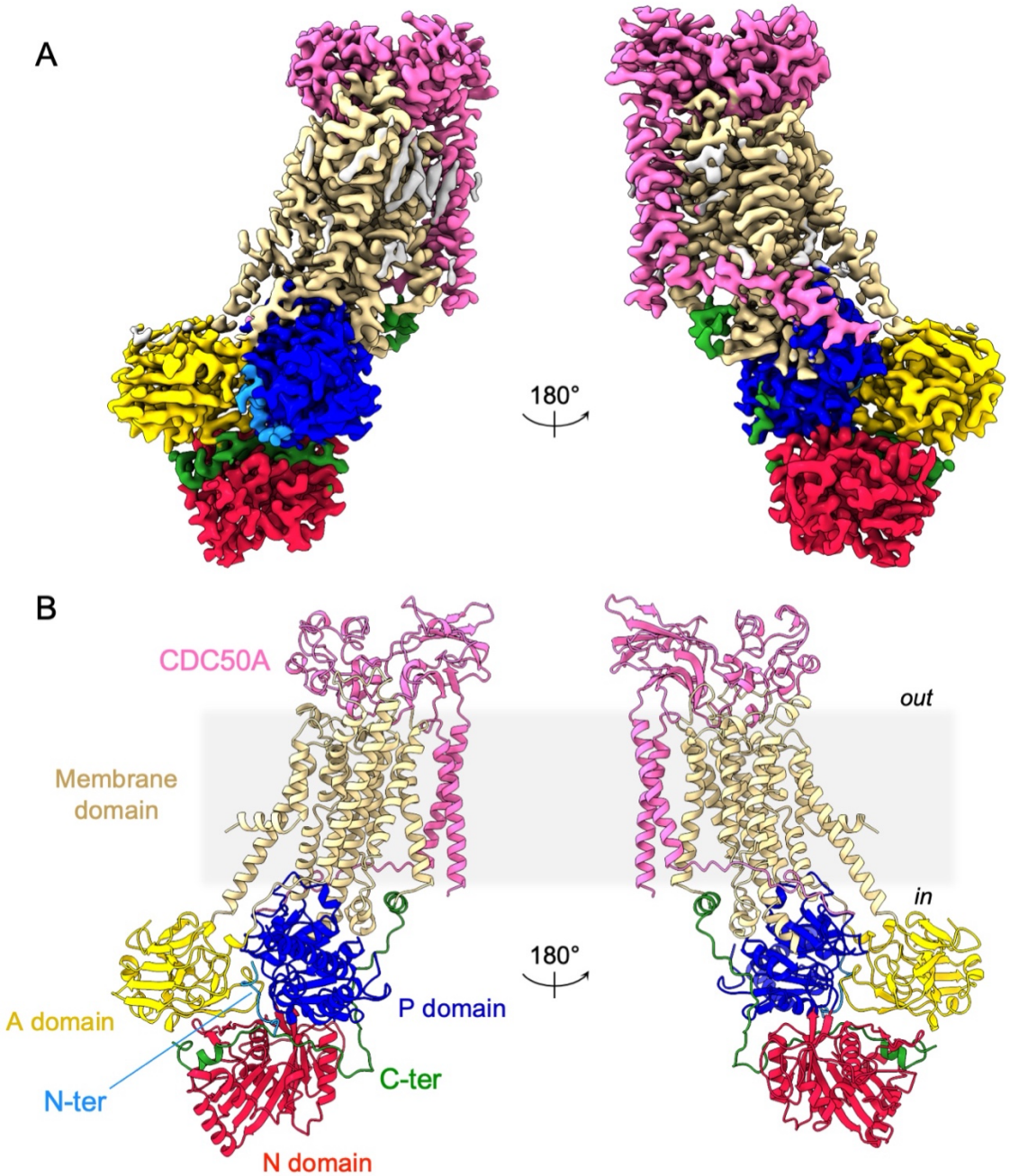

224
225 **Figure 2 – Overall ATP8B1-CDC50A structure.**
226 *(A)* Cryo-EM map of ATP8B1-CDC50A in the E2P autoinhibited state. The cytosolic A-, N- and P-domains of
227 ATP8B1 are colored in yellow, red and blue, respectively. The transmembrane domain of ATP8B1 is colored

in tan. The N- and C-terminal tails of ATP8B1 are colored in cyan and green, respectively. CDC50A is colored in pink. CHS densities and residual densities corresponding to detergent or less ordered unmodelled lipids are in grey. *(B)* Cartoon representation of the refined model. Colors are as in *(A)*. Electron microscopy data bank (EMDB) accession number: EMD-13711. Protein Data Bank (PDB) accession number: 7PY4.

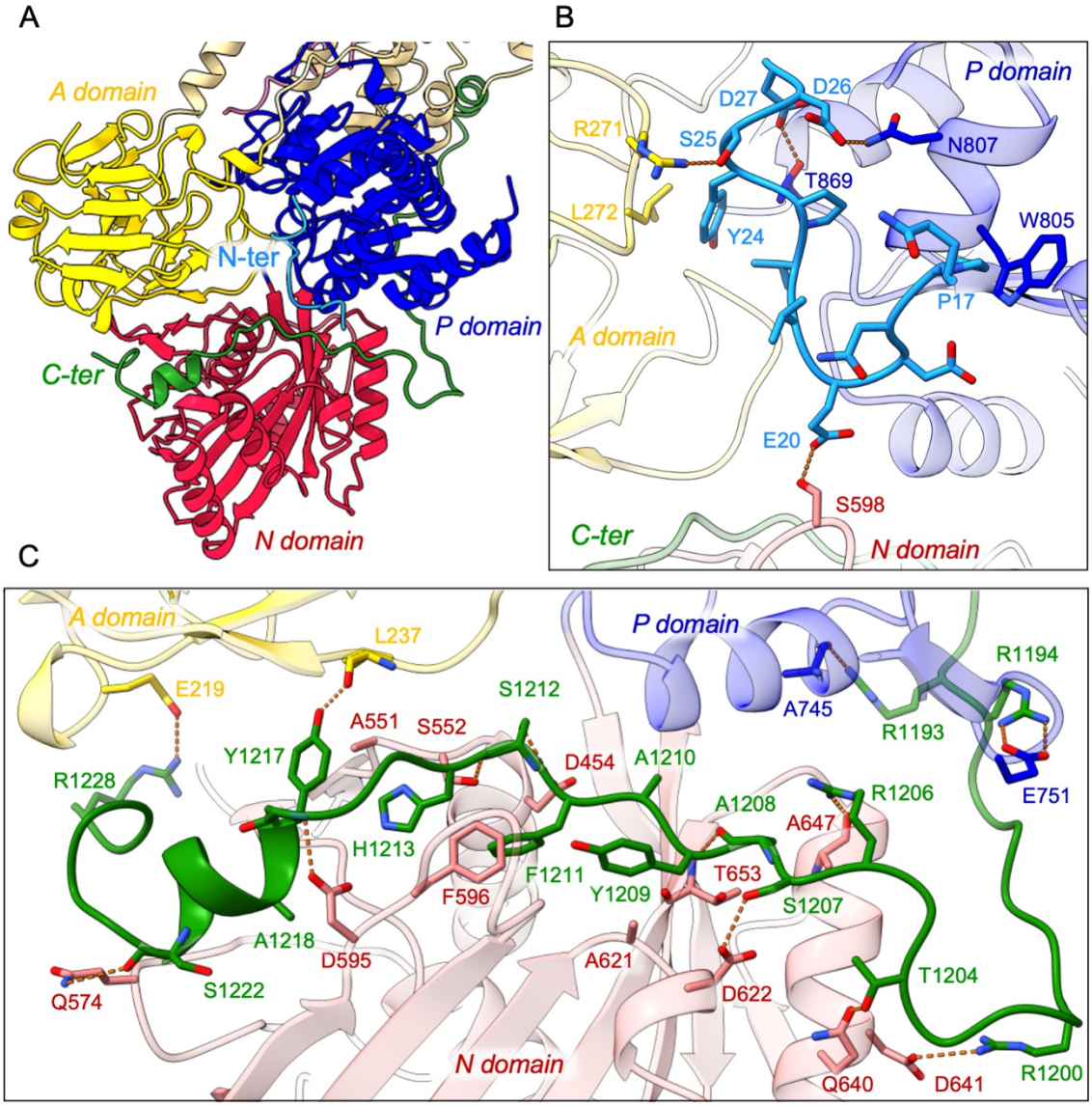

Figure 3 – Detailed interaction of the N- and C-terminal tails with the cytosolic A-, N- and P-domains of ATP8B1.

(A) Overall view of the cytosolic A-, N- and P-domains colored in yellow, red and blue, respectively. The transmembrane domain is colored tan. The N- and C-terminal tails of ATP8B1 are colored in cyan and green, respectively. *(B, C)* Close-up view highlighting the interactions between residues in the N-terminal tail and the cytosolic domains of ATP8B1 *(B)* or the C-terminal tail and the cytosolic domains of ATP8B1 *(C)*. Electrostatic interactions are shown as orange dashes.

245 **Autoinhibition of ATP8B1 by its N- and C-termini**

246 To investigate the role of ATP8B1 N- and C-termini, we inserted 3C protease cleavage sites after
247 residue P42 in the N-terminus, to remove most of the N-terminal tail including the Q16-D27 region
248 found in the structure (ΔN42), and/or after residue E1174 at the end of the last transmembrane
249 segment 10, to remove the C-terminus (ΔC1174 and ΔN42/C1174) (***Figure 4–figure supplement***
250 ***1***). The various 3C protease constructs were purified by streptavidin affinity chromatography (***Figure***
251 ***4A***), with yields ranging from half (for ΔN42), to one fourth (for ΔC1174 and ΔN42/C1174) of that
252 obtained for the wild-type (WT) complex. Noteworthy, insertion of the 3C protease cleavage sites
253 did not alter the interaction between ATP8B1 and CDC50A, as shown by immunoblotting of the
254 fraction collected upon incubation of streptavidin beads with 3C and TEV (***Figure 4–figure***
255 ***supplement 2***). Removal of the N-terminus and/or the C-terminus was not sufficient to stimulate
256 ATP8B1-CDC50A ATPase activity in the presence of its transport substrate PC, suggesting an
257 additional regulatory mechanism (***Figure 4B***). PI(4)P has been shown to be essential to stimulate
258 ATP hydrolysis by Drs2, a yeast homolog of ATP8B1 (Azouaoui et al., 2017). Considering that
259 ATP8B1 is localized at the plasma membrane (PM), we reasoned that addition of PI(4,5)P_2, the most
260 abundant phosphoinositide in the PM (Balla, 2013; Dickson and Hille, 2019), might be required to
261 elicit ATP8B1 activity. While PI(4,5)P_2 proved unable to stimulate the intact WT ATP8B1-CDC50A
262 complex, limited proteolysis of the complex with trypsin dramatically increased the rate of ATP
263 hydrolysis, consistent with autoinhibition of the intact ATP8B1-CDC50A complex (***Figure 4B, Figure***
264 ***4–figure supplement 3***). We observed a ~ four-fold increase of the BeF_x-sensitive ATP hydrolysis
265 upon addition of PI(4,5)P_2 for the C-terminally truncated construct (***Figure 4B***). Interestingly, removal
266 of both termini resulted in additional activation of ATP8B1 suggesting that, although the sole removal
267 of the N-terminus has seemingly no effect on autoinhibition relief, the N-terminus cooperates with
268 the C-terminus for full autoinhibition of the ATP8B1-CDC50A complex (***Figure 4B***). Addition of BeF_x
269 inhibited the ATPase activity of ΔN42/C1174 ATP8B1 with an IC_{50} of ~45 μM, consistent with the
270 ability of this structural analog of phosphate to act as a general P-type ATPase inhibitor (***Figure 4–***
271 ***figure supplement 4A***) (Danko et al., 2009). Finally, the purified ATP8B1-CDC50A complex showed
272 a K_m of ~ 40 μM for MgATP (***Figure 4–figure supplement 4B***).
273

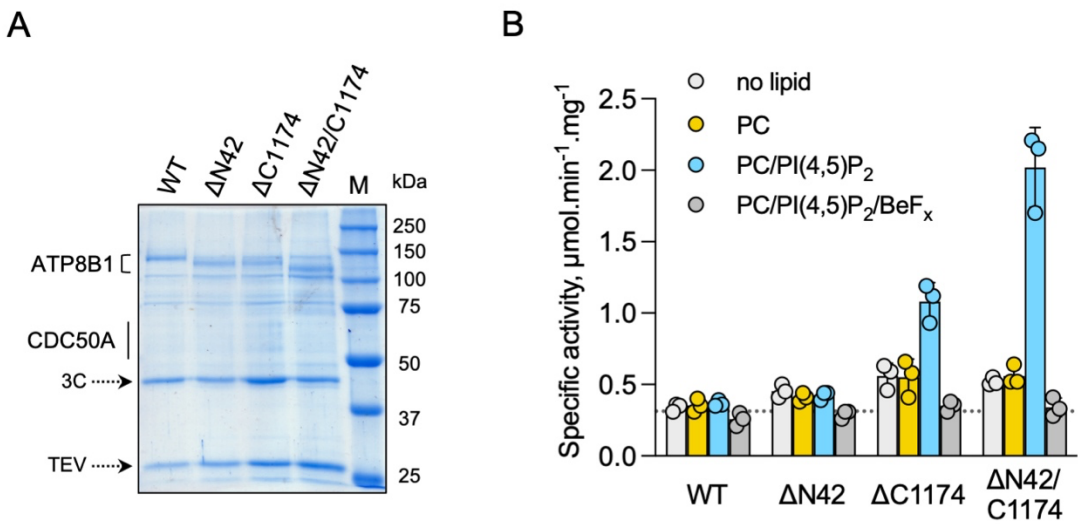

Figure 4 - ATP8B1-CDC50A is autoinhibited by both its N- and C-terminal tails and the presence of lipids is required for its activity.
(A) Removal of N- and/or C-terminal extensions of ATP8B1 upon on-column cleavage of streptavidin-bound ATP8B1-CDC50A with both TEV and 3C proteases assessed by Coomassie blue stained SDS-PAGE. ΔN42 lacks residues 1-42 of ATP8B1 whereas ΔC1174 lacks residues 1175-1251 and ΔN42/C1174 lacks both. M, molecular weight marker. Streptavidin-purified wild-type (WT) and truncated mutants were used for subsequent ATPase assays. *(B)* ATPase activity of wild-type (WT), N-terminally truncated (ΔN42), C-terminally truncated (ΔC1174) and both N- and C-terminally truncated (ΔN42/C1174) ATP8B1 (~ 5 μg ml^{-1} protein) in complex with CDC50A determined in DDM at 30°C. The assay medium contained 1 mM MgATP, 0.5 mg ml^{-1} DDM, and 0.01 mg ml^{-1} CHS. PC and PI(4,5)P_2 were added at 0.1 mg ml^{-1} (132 μM) and 0.025 mg ml^{-1} (23 μM), respectively, resulting in a DDM final concentration of 1.25 mg ml^{-1}. The PC/PI(4,5)P_2 ratio is therefore 5.8 (mol/mol) Data are a mean ± s.d. of 3 technical replicate experiments (purification #1, see Materials and Methods). The dotted line represents background NADH oxidation due to photobleaching, measured in the absence of purified protein and lipids. Source files related to Figure 4B are available in Figure 4 – Source Data 1.

We then asked whether addition of a peptide mimicking the C-terminus of ATP8B1 inhibited the activated enzyme. Of specific relevance, large scale phosphoproteomic studies have shown that mouse ATP8B1 is phosphorylated at residue S1223 (Huttlin et al., 2010; Villén et al., 2007). Given that S1223 is conserved between mouse and human ATP8B1 and that this residue is located at the interface of the A- and the N-domain (***Figure 5A***), we used the non-phosphorylated and phosphorylated versions of the C-terminal peptide to more precisely assess the involvement of the ATP8B1 C-terminal region in autoinhibition and to address the effect of this putative phosphorylation on the autoinhibition mechanism. A peptide encompassing the AYAFS motif (residues 1205-1251, ***Figure 4 – figure supplement 1***) was chemically synthesized and incubated with ΔN42/C1174 ATP8B1. The C-terminal peptide efficiently inhibited ATP hydrolysis by ATP8B1, with an IC_{50} of ~ 22 μM (***Figure 5B, Figure 5D, and Table 2***), without adversely impacting proper functioning of the enzyme-coupled assay (***Figure 5 – figure supplement 1***).

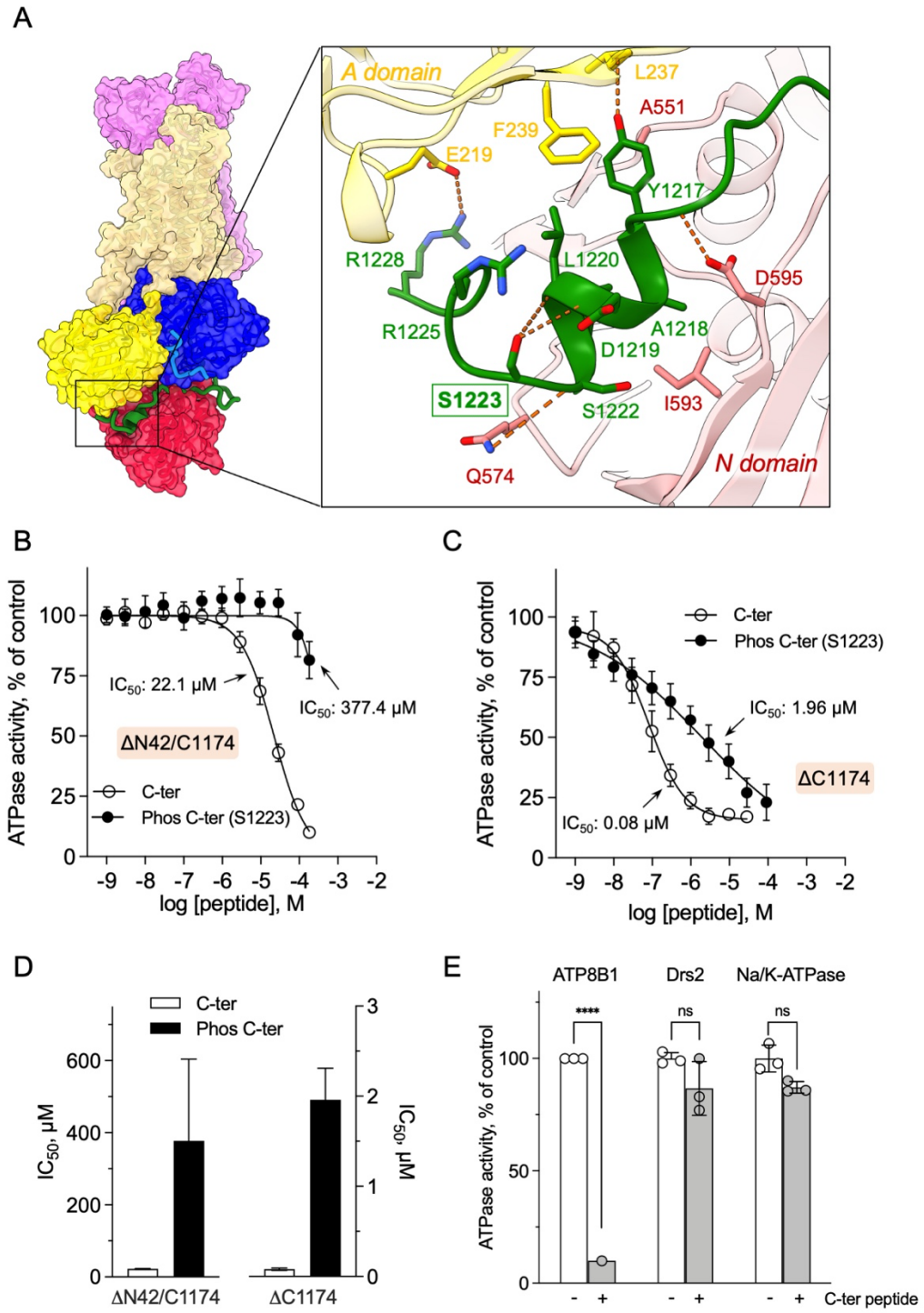

Figure 5 – Autoinhibition of ATP8B1 by its N- and C-terminal extensions.
(A) Overall and close-up views of S1223 in the cleft formed by the A- and N-domains. The cytosolic A- and N-domains of ATP8B1 are colored in yellow and red, respectively, and are shown as surface and cartoon. The C-terminal tail of ATP8B1 is shown as cartoon with side chains in green. Electrostatic interactions are shown as orange dashes. *(B)* Back-inhibition of ΔN42/C1174 ATP8B1 (~ 3-3.3 μg ml^{-1} protein) by synthetic C-terminal peptides (C-ter, Phos C-ter). ATPase activity was determined at 37°C. The BeF_x-sensitive ATPase activity is plotted, taking the activity in the absence of the C-terminal peptide as 100%. The data were fitted to an inhibitory dose-response equation with variable slope. 95% confidence intervals for IC_{50} values are given as CI[lower CI, upper CI]. C-terminal peptide: CI[1.98x10^{-5}, 2.48x10^{-5}]; phosphorylated C-terminal peptide:

CI[1.44x10^{-4}, 9.90x10^{-4}]. Data are mean ± s.d. of 3 replicate experiments (purification #2, see Materials and Methods). *(C)* Back-inhibition of ΔC1174 (~ 3-3.3 μg ml^{-1} protein) by C-terminal peptides. ATPase activity was determined at 37°C. The BeF_x-sensitive ATPase activity is plotted, taking the activity in the absence of C-terminal peptide as 100%. The data were fitted to an inhibitory dose-response equation with variable slope. C-terminal peptide: CI[5.86x10^{-8}, 1.12x10^{-7}]; phosphorylated C-terminal peptide: CI[1.40x10^{-6}, 2.73x10^{-6}].Data are a mean ± s.d. of 3-4 replicate experiments (purification #2, see Materials and Methods). For panels *(B)* and *(C)*, the assay medium contained 1 mM MgATP, 0.5 mg ml^{-1} DDM, and 0.01 mg ml^{-1} CHS. PC and PI(4,5)P_2 were added at 43 μg ml^{-1} (43 μM) and 0.025 mg ml^{-1} (23 μM), respectively. *(D)* Half-maximal inhibitory concentration (IC_{50}) of ATP8B1-CDC50A ATPase activity by C-terminal peptides deduced from curves in (*B*) and (*C*). Error bars represent the mean ± s.d. based on 33 to 47 data points. *(E)* Specificity of ATP8B1 inhibition by its C-terminal tail. ATPase activity of purified DDM-solubilized Drs2-Cdc50 (20 μg ml^{-1}) and pig α1β1 Na^+/K^+-ATPase (10 μg ml^{-1}) in microsomal membranes was determined at 30°C and 37°C, respectively, in the absence or presence of 180 μM ATP8B1 C-terminal peptide. The results shown in this panel for ATP8B1 inhibition are the same as those displayed in panel *(B)* for a concentration of 180 μM C-terminal peptide. The rate of ATP hydrolysis was corrected for NADH photobleaching and the activity in the absence of the C-terminal peptide was taken as 100% for each species. **** $P < 0.0001$ according to two-way ANOVA with Tukey's test vs activity in the absence of peptide. ns: not significant. Data are a mean ± s.d. of 3 replicate experiments. Source files for Figure 5B, 5C, 5D and 5E are available in Figure 5 – Source Data 1, Figure 5 – Source Data 2, Figure 5 – Source Data 3 and Figure 5 – Source Data 4, respectively.

Remarkably, phosphorylation at S1223 impaired the ability of the C-terminal peptide to inhibit ΔN42/C1174 ATP8B1, with an IC_{50} shifted to approximately 380 μM (***Figure 5B, Figure 5D and Table 2***). Furthermore, inhibition of ΔC1174 ATP8B1, i.e. still containing the N-terminal tail, was about 270-fold more efficient (IC_{50} ~ 0.08 μM) than ΔN42/C1174. Similar to the effect on the ΔN42/C1174 variant, phosphorylation at S1223 decreased the ability of the C-terminal peptide to inhibit ATPase activity of the ΔC1174 ATP8B1 variant (***Figure 5C, Figure 5D and Table 2***). These results strongly support a prominent role for the N-terminal tail of ATP8B1 in the autoinhibition mechanism. Importantly, inhibition was specific as neither the yeast P4-ATPase Drs2, nor the cation-transporting Na^+/K^+-ATPase (a P2-ATPase), could be inhibited by the C-terminal tail of ATP8B1 (***Figure 5E***).

Together, our data reveal that the ATP8B1-CDC50A flippase is autoinhibited by its N- and C-terminal extensions in a cooperative mechanism and that PI(4,5)P_2 is a major regulator of its activity.

ATP8B1-CDC50A	Inhibitory peptide	IC_{50} (μM)
ΔN42/C1174 (*n* = 33)	C-terminal	22.1 ± 1.2
ΔN42/C1174 (*n* = 35)	Phosphorylated C-terminal	377.4 ± 227
ΔC1174 (*n* = 34)	C-terminal	0.081 ± 0.014
ΔC1174 (*n* = 47)	Phosphorylated C-terminal	1.96 ± 0.35

354
355 **Table 2: Half-maximal inhibitory concentration (IC50) values for the C-terminal peptide, in comparison**
356 **with its phosphorylated form.** The values indicated in the table were deduced from dose-response curves
357 displayed in Figure 5B and Figure 5C. The number of data points used to calculate the IC50 is indicated in
358 parenthesis. IC50 values are expressed as mean ± s.d.
359

360 **Lipid-dependence of ATP8B1 activity**

361 We showed that ATP8B1-CDC50A required PC and PI(4,5)P_2 for enzyme turnover (***Figure 4B***). We
362 next explored the effect of other lipid species on the enzyme turnover in the presence of PI(4,5)P_2.
363 Under these conditions, PE and to a lesser extent PS, but not cardiolipin (CL) and sphingomyelin
364 (SM) could stimulate ATP8B1 activity (***Figure 6A***). Plasma-membrane localized yeast P4-ATPases
365 Dnf1 and Dnf2 have been shown to transport lyso-phosphatidylcholine (Lyso-PC) (Riekhof et al.,
366 2007) and the alkylphosphocholine analogs miltefosine and edelfosine (Hanson et al., 2003), in
367 addition to PC (Pomorski et al., 2003). Furthermore, when co-expressed with CDC50A, murine
368 ATP8B1 was shown to increase uptake of the alkylphosphocholine analog perifosine in HeLa and
369 HEK293T cells (Muñoz-Martínez et al., 2010). As compared with background levels, Lyso-PC
370 induced a clear increase in the ATP hydrolysis rate of ΔN42/C1174 ATP8B1. Weak activation was
371 also observed in the presence of edelfosine and miltefosine (***Figure 6A***).
372

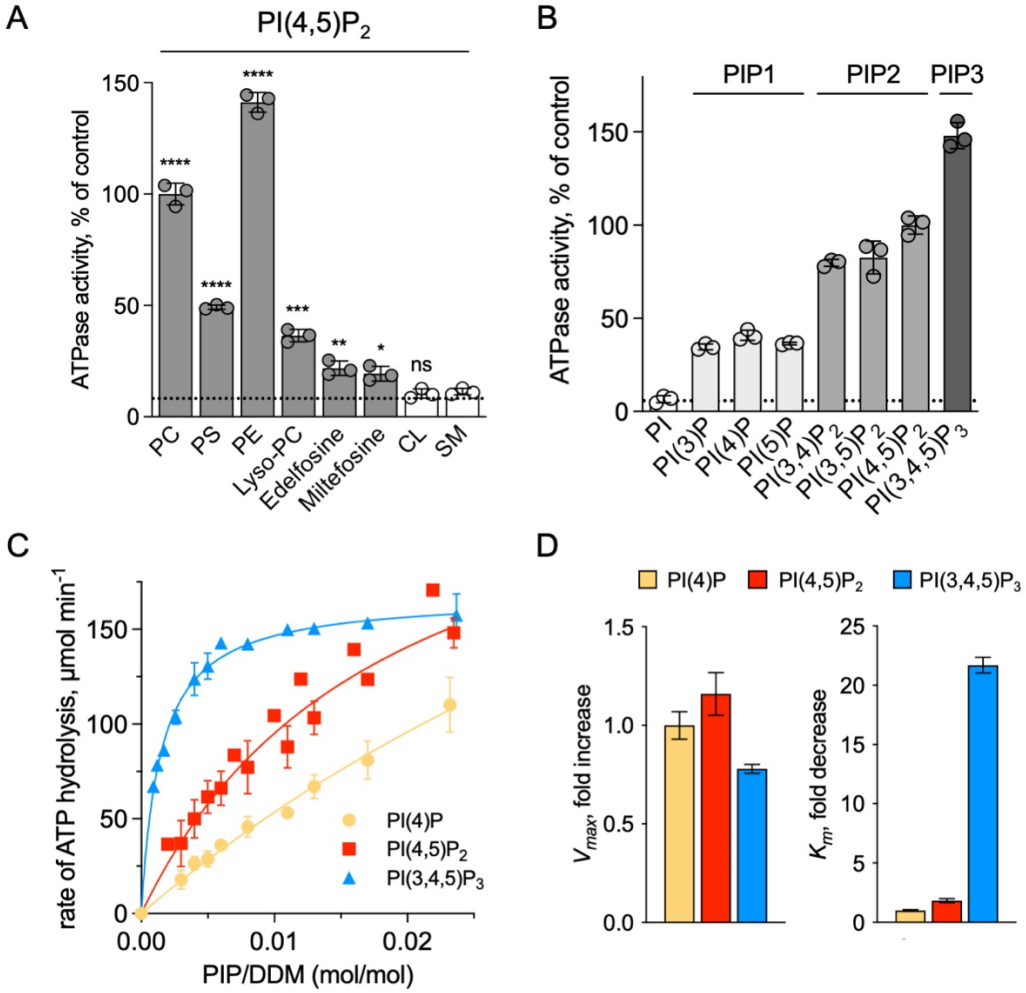

Figure 6 – Sensitivity of ATP8B1-CDC50A to phospholipids.
(A) ATPase activity of the ΔN42/C1174 ATP8B1 determined in the presence of various glycerophospholipids, lipid derivatives, and sphingomyelin, at 30°C. The assay medium contained 1 mM MgATP, 1 mg ml^{-1} DDM, and 0.01 mg ml^{-1} CHS. PI(4,5)P_2 was added at 23 μM and the various lipids and lipid derivatives were added at 115 μM. The rate of ATP hydrolysis was corrected for NADH photobleaching occurring before the addition of the purified ATP8B1-CDC50A complex to the assay cuvette. The specific activity measured in the presence of PC and PI(4,5)P_2 was taken as 100% (~0.15-0.3 μmol min^{-1} mg^{-1}). The dotted line represents the background activity measured in the absence of any added lipid. **** $P < 0.0001$, *** $P = 0.0002$, ** $P = 0.0071$, * $P = 0.0177$ according to unpaired two-tailed *t* test *vs* SM condition. ns: not significant. Data are mean ± s.d. of 3 replicate experiments. *(B)* ATPase activity of the ΔN42/C1174 ATP8B1 (0.5 μg ml^{-1}) determined in the presence of mono, di, and tri-phosphorylated phosphoinositides, at 30°C. The activity was measured in the presence of 1 mg ml^{-1} DDM, 0.1 mg ml^{-1} CHS, 115 μM PC and 23 μM of the indicated phosphoinositides. The rate of ATP hydrolysis was corrected for NADH photobleaching occurring before the addition of the purified ATP8B1-CDC50A complex and ATP to the assay cuvette. The specific activity of the wild-type measured in the presence of PC and PI(4,5)P_2 was taken as 100%. The dotted line represents the activity measured in the sole presence of PC. Data are mean ± s.d. of 3 replicate experiments. *(C)* Apparent affinity of ΔN42/C1174 ATP8B1 (~ 3-3.3 μg ml^{-1}) for PI(4)P, PI(4,5)P_2 and PI(3,4,5)P_3. K_m for phosphoinositides was measured at 37°C in the presence of PC. The assay medium contained 1 mM MgATP, 0.5 mg ml^{-1} DDM, 0.01 mg ml^{-1} CHS, 23 μM PI(4,5)P_2 and 57 μM PC. Successive additions of DDM and PC gradually decreased the PI(4,5)P_2/DDM ratio. The PC/DDM ratio remained constant at 0.058 mol/mol. Plotted lines represent the best fit to a Michaelis-Menten equation. *(D)* Variations of the maximum velocity (V_{max}) and apparent affinity (K_m) of ΔN42/C1174

ATP8B1 for phosphoinositides calculated from double reciprocal plots displayed in ***Figure 6 – figure supplement 1***, with respect to that measured in the presence of PI(4)P. The data in *(C)* and *(D)* represent the mean ± s.d. of 3-4 replicate experiments. Source files for Figure 6A, 6B, 6C and 6D are available in Figure 6 – Source Data 1, Figure 6 – Source Data 2, Figure 6 – Source Data 3 and Figure 6 – Source Data 4, respectively.

To further dissect the regulatory mechanism of ATP8B1-CDC50A, we examined the specificity of the purified enzyme for PPIns. All PPIn species were tested at the same molar concentration and at a fixed concentration of PC, and differed in the number and positions of phosphorylations on the inositol headgroup. Phosphorylation of the headgroup appeared to be essential for stimulating ATP8B1 ATPase activity, as no activity could be detected above background using phosphatidylinositol (***Figure 6B***). Monophosphorylated PPIn species, namely PI(3)P, PI(4)P, and PI(5)P, were equally efficient in stimulating ATP hydrolysis by ATP8B1. When the inositol ring was phosphorylated twice, the ATPase activity was increased about 2-fold compared to that observed with monophosphorylated PPIns (***Figure 6B***), with no dramatic difference in activity between PI(4,5)P_2, PI(3,4)P_2, and PI(3,5)P_2. Tri-phosphorylated PI(3,4,5)P_3 increased further the activity of ATP8B1 by about 1.5 fold. Thus, although the number of phosphorylations on the inositol ring matters, the positions do not and ATP8B1-CDC50A can be activated by a wide variety of PPIns with increasing efficiency linked to the number of phosphorylations. The differential activation by PPIns observed in ***Figure 6B*** could either be the result of a variation in the maximal velocity of ATP hydrolysis, the apparent affinity for PPIns, or both. To distinguish between these possibilities, we measured the rate of ATP hydrolysis by ATP8B1 in relation to the PPIn/detergent ratio (***Figure 6C***), taking PI(4)P, PI(4,5)P_2 and PI(3,4,5)P_3 as representative examples of singly, doubly and triply phosphorylated PPIns, respectively. Whereas double-reciprocal plots indicated comparable maximum ATP hydrolysis rates in the presence of PI(4)P, PI(4,5)P_2 and PI(3,4,5)P_3, the apparent affinity of ATP8B1 for PI(3,4,5)P_3 was found much higher than for PI(4)P and PI(4,5)P_2 (***Figure 6D, Figure 6–figure supplement 1***). Thus, ATP8B1 exhibits a strong preference for PI(3,4,5)P_3 over other PPIns *in vitro*.

425 **Discussion**

426

427 Based on the cryo-EM structure of ATP8B1-CDC50A and dissection of its regulatory mechanism
428 using biochemical assays, we identify the C-terminal extension of ATP8B1 as a central component
429 in the regulation of its activity, and a cooperative contribution of the N-terminus of ATP8B1 in the
430 autoregulatory mechanism. Furthermore, we report that PPIns are essential activators of ATP8B1
431 activity and identify *in vitro* a preference for PI(3,4,5)P_3 in the activation of ATP8B1. Truncation of
432 the C- and N-termini of ATP8B1 allows switching ATP8B1 from a fully inhibited to an activated form,
433 provided lipid transport substrate and PPIns are present. Addition of a C-terminal peptide rescues
434 inhibition, and inhibition is subject to regulation by phosphorylation at S1223 of the C-terminal
435 extension.

436

437 **Autoinhibition of P4-ATPase flippases by their terminal tails: an evolutionarily conserved**
438 **mechanism? –** The autoinhibition of plasma membrane-localized ATP8B1 by its C-terminus is
439 reminiscent of that observed for the yeast endomembrane homolog Drs2. While an intact Drs2-
440 Cdc50 complex exhibits hardly any lipid-induced ATPase activity, once the C-terminus has been
441 trimmed off by proteases, the complex becomes competent for ATP hydrolysis (Azouaoui et al.,
442 2017). The ability of Drs2 to hydrolyze ATP requires not only displacement of its C-terminus but also
443 the binding of PI(4)P (Azouaoui et al., 2017; Timcenko et al., 2019). Cryo-EM structures show that
444 the C-terminus of Drs2 binds in a cleft between the P-domain and the N-domain, thus providing a
445 structural explanation for autoinhibition (Bai et al., 2019; Timcenko et al., 2019). The C-terminus also
446 appears to play a role in autoinhibition of ATP8A2, although this enzyme does not seem to be
447 regulated by PPIns (Chalat et al., 2017). In particular, the C-terminus of ATP8A1, a close relative of
448 ATP8A2, was recently shown to extend through its cytosolic catalytic domains (Hiraizumi et al.,
449 2019). This raises the question as to whether such autoregulatory mechanism is a conserved feature
450 among P4-ATPases. By comparing the sequences of P4-ATPase termini from various organisms
451 (***Figure 7A, Figure 4–figure supplement 1*** for a full alignment), it appears that although the C-
452 termini of P4-ATPases are in general poorly conserved, one exception to this rule is the ATP8B1
453 AYAFS motif which occupies the ATP binding site. Furthermore, in the autoinhibited Drs2 and
454 ATP8A1 structures, their C-termini overlap extensively despite a rather low sequence conservation
455 (***Figure 7B***). Noteworthy, the C-terminal peptide of ATP8B1 did not exhibit an inhibitory effect on
456 Drs2 (***Figure 5E***), suggesting that autoinhibition per se is mainly driven by the region downstream
457 the conserved motif, the latter mediating the interaction between the A and N domain. Thus, we
458 predict that any P4-ATPase containing the (G/A)(Y/F)AFS motif is likely to be autoinhibited by its C-
459 terminus. We further propose that autoinhibition might be occurring in a conformation-dependent

460 manner. Indeed, previous structural work from Hiraizumi and colleagues, capturing an almost
461 complete catalytic cycle of full-length ATP8A1-CDC50A, showed that the inhibitory C-terminus is
462 observed only in the BeF_x-stabilized E2P form and is completely disordered in other conformations,
463 suggesting that autoinhibition specifically occurs in the E2P state. We also show in Figure 1D that
464 full-length ATP8B1 may be phosphorylated from [γ-^{32}P]ATP, indicating that in the E1 state, the
465 presence of the C-terminal tail does not prevent accessibility of the nucleotide-binding site. As such,
466 we foresee that the C-terminal tail is in equilibrium between a state bound to the ATP8B1 cytosolic
467 domains and an unbound state, this equilibrium being poised toward the bound state in the E2P
468 conformation.
469

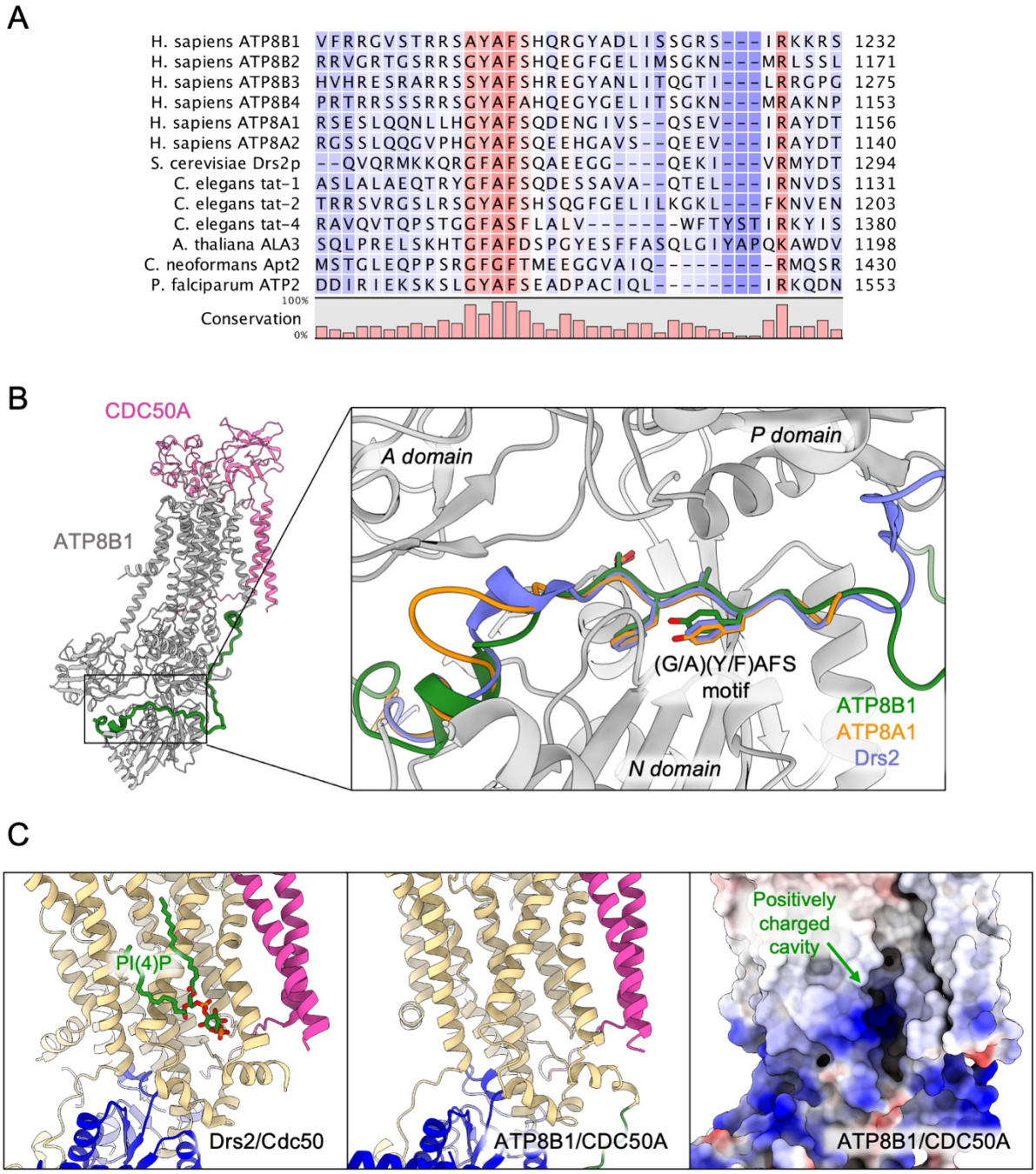

Figure 7 – Proposed mechanism for autoinhibition and regulation by phosphoinositides of the ATP8B1-CDC50A complex.

(A) Sequence alignment of select P4-ATPases C-termini, including ATP8B1, ATP8A1 and Drs2, which are all known to be autoinhibited. The shading indicates conservation (blue 0% – red 100%). *(B)* Comparison of the binding sites of ATP8B1, ATP8A1 (PDB ID: 6K7N) and Drs2 (PDB ID: 6ROH) C-terminal tails, respectively in green, orange and blue reveals a common architecture and location of the inhibitory C-termini, and specifically the conserved (G/A)(Y/F)AFS motif (AYAFS for ATP8B1, GYAFS for ATP8A1 and GFAFS for Drs2) located in the ATP binding pocket. *(C)* Side view of the PI(4)P-binding site of Drs2 (left). PI(4)P (in stick representation) is bound in the membrane domain. The same region in ATP8B1 reveals a similar organization (middle) with the presence of a positively-charged cavity (right) suggesting a putative phosphoinositide binding pocket in ATP8B1. CDC50A and Cdc50 transmembrane helices are colored in pink.

483
484
485 Our study also identifies a previously unrecognized role for the N-terminal tail of ATP8B1 in the
486 autoinhibition process. Although the precise mechanism is so far uncertain, our data indicate that
487 the N-terminal tail of ATP8B1 has a strong synergistic effect on the autoinhibition by its C-terminal
488 extension (***Figure 4B***, ***Figure 5B-D***). Owing to numerous interactions observed in our structure of
489 ATP8B1, the N-terminal tail might restrain the flexibility of the A-, N- and P-domains necessary for
490 nucleotide binding to the N-domain and catalysis, even in the absence of the C-terminal tail. Another
491 non-exclusive possibility could be that the N-terminal tail prevents dissociation of the C-terminus by
492 locking down the N-domain through electrostatic interaction with S598. A functional cooperation
493 between N- and C-termini has previously been described for the plant H^+-ATPase, a P-type ATPase
494 from the P3 subfamily, where modifications in the N-terminus result in kinase-mediated
495 phosphorylation in the C-terminus, eventually leading to activation of the pump (Ekberg et al., 2010).
496 Moreover, recent cryo-EM structures revealed an autoinhibitory role for the N-terminus of the P5B-
497 ATPase Ypk9 mediated by its interaction with the cytosolic domains (***Figure 7–figure supplement***
498 ***1***), and it was proposed in this study that the C-terminal tail of Ypk9 may also play a functional role
499 owing to its interaction with the P-domain (Li et al., 2021).
500
501 **Phosphorylation as a mechanism for the regulation of ATP8B1 activity –** The inhibitory
502 properties of a peptide derived from the C-terminus of ATP8B1 suggest that phosphorylation of
503 residue S1223 plays an important role. Identification of the corresponding residue (S1223) from the
504 mouse orthologue ATP8B1 in large-scale phosphoproteomic studies (Huttlin et al., 2010; Villén et
505 al., 2007), suggests that phosphorylation of S1223 in human ATP8B1 might be part of the activating
506 mechanism that lifts autoinhibition *in vivo*. Consistent with this hypothesis, calcium/calmodulin-
507 dependent protein kinase II (CaMKII) has been shown to phosphorylate a serine residue, S1138, in
508 the autoinhibitory C-terminus of bovine ATP8A2. Substitution of S1138 to alanine resulted in a 33%
509 loss of the PS-dependent ATPase activity of ATP8A2 (Chalat et al., 2017). Canalicular transporters
510 also involved in inherited forms of intrahepatic cholestasis such as the bile salt export pump (PFIC2,
511 ABC11B) have been found phosphorylated by PKC when overexpressed in insect cells (Noe et al.,
512 2001) and the floppase ABCB4 (PFIC3), known to transport PC in the opposite direction compared
513 to ATP8B1, was shown to be stimulated by PKA- and PKC-dependent phosphorylation (Gautherot
514 et al., 2014). Future studies are required to identify kinases responsible for the phosphorylation of
515 S1223 and other sites, to investigate the functional consequences of ATP8B1 phosphorylation on
516 its activity, both *in vitro* and in *vivo*.
517

518 **Regulation of ATP8B1-CDC50A by phosphoinositides** – In this study, we identified PPIns as
519 regulators of ATP8B1 ATPase activity. It must be pointed out that the activity of the intact full-length
520 ATP8B1 is not stimulated by addition of PI(4,5)P_2 (***Figure 4B***) and that the C-terminus of ATP8B1
521 must be removed for PI(4,5)P_2 to exert its stimulatory effect. While it remains possible that
522 phosphoinositides participate in autoinhibition relief, as proposed for the yeast Drs2-Cdc50 flippase
523 complex, this suggests that phosphoinositides mediate their activatory effect through a distinct
524 mechanism that does not involve the tails, e.g. by promoting conformational changes in the
525 membrane domain that could for instance regulate access to the substrate-binding site. Whereas all
526 PPIns showed the ability to stimulate ATP8B1 activity (***Figure 6***), PI(3,4,5)P_3 displayed a much
527 higher affinity for ATP8B1 than other PPIns. The K_m value for activation of ATP8B1 by PI(3,4,5)P_3 is
528 about $1.4.10^{-3}$ mol PI(3,4,5)P_3/mol DDM. Based on our own estimation of the number of DDM
529 molecules surrounding the transmembrane domain of Drs2-Cdc50 using size-exclusion
530 chromatography in the presence of ^{14}C-labeled DDM (***Figure 6 – figure supplement 2***), we estimate
531 that the detergent micelle around the transmembrane region of ATP8B1-CDC50A is composed of ~
532 270 ± 56 molecules of DDM. Taking into account the additional presence of two transmembrane
533 helices contributed by Cdc50, this is the same order of magnitude as the amount of DDM bound to
534 purified SERCA1a (155 ± 27 mol DDM/mol SERCA1a), a P-type ATPase from the P2 subfamily, as
535 determined by MALDI-TOF mass spectrometry (Chaptal et al., 2017). A K_m value of $1.4x10^{-3}$ mol
536 PI(3,4,5)P_3/mol DDM corresponds to ~0.38 mol of PI(3,4,5)P_3 per 270 mol of DDM (or 0.14 mol%)
537 in the immediate environment of ATP8B1-CDC50A, emphasizing the strong affinity of ATP8B1 for
538 PI(3,4,5)P_3. This is consistent with PPIns being activators rather than substrates as is the case for
539 PI(4)P towards the yeast Drs2-Cdc50 complex. PI(3,4,5)P_3 is primarily localized at the plasma
540 membrane, and one of the least abundant PPIns in mammalian cells, being virtually undetectable in
541 quiescent cells. The tight control of PI(3,4,5)P_3 concentration stems from its critical role in key
542 signalling pathways such as cell proliferation, survival and membrane trafficking (Marat and Haucke,
543 2016). Interestingly, a recent report provided quantitative analysis of phosphoinositides, including
544 PI(3,4,5)P_3, in the plasma membrane of MT-4 cells, a T-lymphocyte cell line. In these cells,
545 PI(3,4,5)P_3 represents 0.00025% of total plasma membrane lipids (Mücksch et al., 2019). However,
546 upon activation of cell-surface receptors and recruitment of class I PI3-kinases, PI(3,4,5)P_3 levels
547 may rise up to 100-fold (Clark et al., 2011), suggesting that its concentration may rise up to 0.025
548 mol% in the PM. Although comparison must be made with care, due to the fact that activation of
549 ATP8B1 by PI(3,4,5)P_3 may be different in lipid bilayer and solubilized systems, it is worth noting that
550 0.025 mol% of PI(3,4,5)P_3 in the PM is in the same range as 0.14 mol%, the PI(3,4,5)P_3 concentration
551 required to reach half-maximal activity of ATP8B1 in detergent micelles.

552 The lower K_m of ATP8B1 for PI(3,4,5)P_3 than for other PPIns suggests that the cavity where
553 PI(3,4,5)P_3 binds is specifically adjusted to this PPIn, whereas other PPIns can fit as well, but less
554 efficiently. To our knowledge, direct regulation of integral membrane proteins by PI(3,4,5)P_3 has not
555 previously been shown. Intriguingly, despite addition of PI(3,4,5)P_3 during sample preparation for
556 cryo-EM studies, no clear density could be observed for this lipid. However, the cavity lined by TM7,
557 TM8 and TM10 on the structure of ATP8B1, which corresponds to the PI(4)P binding site in Drs2,
558 consists of a large number of basic residues (***Figure 7C***) strongly hinting at a similar site in both
559 Drs2 and ATP8B1. On the other hand, the role of PPIns on the activation of ATP8B1 with C-terminal
560 or double N- and C-terminal truncation could be interpreted as supporting a model where regulatory
561 PPIns bind to the N-terminal tail of ATP8B1. Interestingly, the N-terminal tail of ATP8B1 contains a
562 patch of positively charged residues between P42 and D70 (including R46, R49, R55, R59 and K60),
563 a region which is not visible in our structure. This would be reminiscent of the proposed model for
564 the P5-ATPase ATP13A2, where binding of the negatively charged lipids phosphatidic acid and
565 PI(3,5)P_2 to the N-terminal domain stimulates catalytic activity (Holemans et al., 2015; Tomita et al.,
566 2021).
567 Irrespective of this, the physiologically relevant regulatory PPIn is still unknown. Given the
568 localization of ATP8B1 in the apical membrane of epithelial cells in mammals, and the subcellular
569 localization and abundance of PPIns in cell membranes (Balla, 2013; Dickson and Hille, 2019), both
570 PI(3,4,5)P_3 and PI(4,5)P_2 might fulfill this task. Future studies aimed at manipulating PPIns levels in
571 living cells should help reveal whether ATP8B1 depends on specific PPIns *in vivo*, opening the way
572 to modulate functional levels of ATP8B1 in cells.
573
574 **Structural basis for catalytic deficiency induced by inherited ATP8B1 mutations** – Our
575 structural model of ATP8B1 enabled us to map the mutations found in patients suffering from PFIC1,
576 BRIC1 or ICP1 (Bull et al., 1998; Deng et al., 2012; Dixon et al., 2017; Klomp et al., 2004; Painter et
577 al., 2005) (***Figure 8A***). Mutations are homogenously distributed along the protein sequence, and
578 some mutations are likely to impair catalytic properties of ATP8B1 directly (***Figure 8B***). Mutations
579 D554N and H535L are located in the nucleotide binding pocket, suggesting that these mutations
580 might prevent or affect ATP binding. The D554 residue is at interacting distance with the
581 autoinhibitory C-terminus and its mutation might also alter autoregulation. Additionally, mutations
582 S453Y, D454G and T456M in the P-domain will abolish autophosphorylation of the catalytic
583 aspartate (D454), thus resulting in an inactive ATP8B1.
584

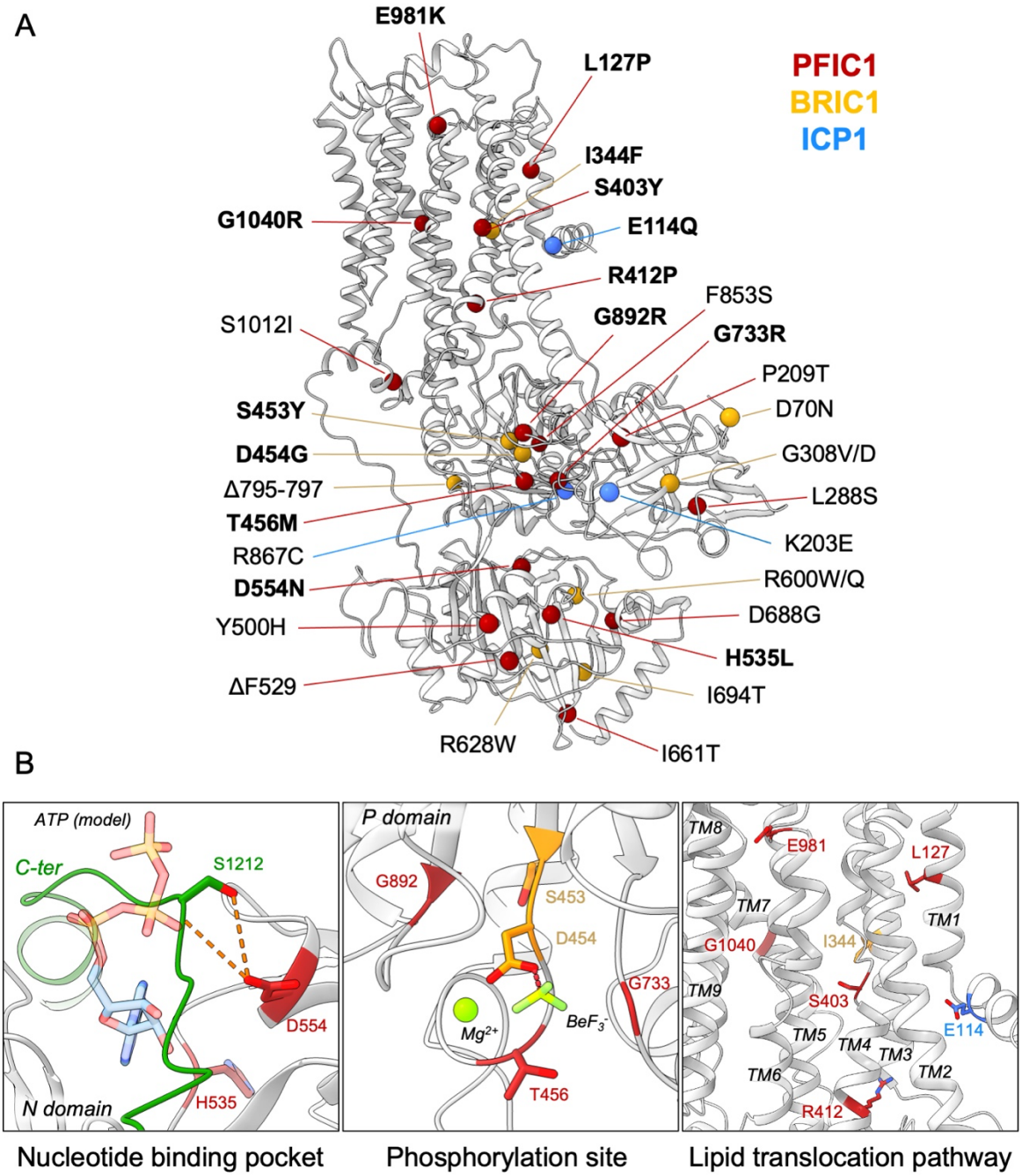

Figure 8 – Structural map of the inherited intrahepatic disease-related mutations.
(*A*) Mutations found in PFIC1, BRIC1 or ICP1 patients are respectively shown as red, yellow and blue spheres on ATP8B1 $E2P_{autoinhibited}$ structure (in grey). Mutations indicated in bold are presented in panel *(B)*. *(B)* Close-up views of the nucleotide binding site within the N-domain of ATP8B1. The ATP molecule position was model by aligning ATP8B1 N domain with the N domain of ATP8A1 in E1-ATP bound state (PDB: 6K7J) (left). (Middle) the phosphorylation site in the P-domain with Mg^{2+} and the phosphate mimic BeF_3^- in green. (Right) the lipid transport pathway.

The structure of ATP8B1 presented in this report is locked in a $E2P_{autoinhibited}$ state where the exoplasmic lipid pathway is closed. However, it is important to note that numerous mutations can be

597 found in this region (***Figure 8B***). In particular, the S403 residue, mutated to a tyrosine in PFIC1, is
598 part of the PISL motif conserved in P4-ATPases. The PISL motif is located in TM4 and has been
599 shown to interact with the phosphoglycerol backbone of PS, the transport substrate of Drs2 and
600 ATP8A1 (Hiraizumi et al., 2019; Timcenko et al., 2021). A relatively conservative mutation of this Ser
601 into Ala in ATP8A2 (S365A), has been shown to significantly diminish its ATPase activity and
602 transport substrate affinity (Vestergaard et al., 2014). Moreover, mutations E981K and L127P have
603 also been shown to impair ATP8B1-catalyzed transport of PC *in vivo* (Takatsu et al., 2014). Mutation
604 of the corresponding residues in the PS-specific ATP8A2 alters ATPase activity and lipid specificity
605 (Gantzel et al., 2017). Further functional and structural studies will be needed to better understand
606 how these mutations may affect substrate recognition and translocation.
607
608 **Conclusions –** Our findings show that the plasma membrane P4-ATPase ATP8B1 is tightly
609 regulated by its N- and C-terminal tails as well as PPIns and that the autoinhibitory mechanism can
610 be mimicked by exogenous peptides. Understanding the regulatory mechanism of mammalian P4-
611 ATPases will be instrumental for the subsequent design of molecules that would enforce/mimic or
612 stimulate the release of the autoinhibitory C-terminus. We propose that the regulatory mechanism
613 uncovered in this study may be a feature shared by other P4-ATPases, and that phosphorylation of
614 the C-terminal tail of ATP8B1 is likely to be involved in the regulation of ATP8B1 activity. Moreover,
615 these studies will pave the way towards detailed functional assessment of disease-associated
616 ATP8B1 mutations found in PFIC1 patients and towards the design of both activating and inhibiting
617 compounds of P4-ATPases, based on regulatory mechanisms *in vivo*.
618

619 **Materials and Methods**

620

Key Resources Table				
Reagent type (species) or resource	**Designation**	**Source or reference**	**Identifiers**	**Additional information**
gene (include species here)				
strain, strain background (include species and sex here)	W303.1b/ *Δpep4*	López-Marqués laboratory		Strain deficient for the main vacuolar protease
strain, strain background (include species and sex here)	W303.1b/ *GAL4-2*	Pompon Laboratory		Additional copy of the *GAL4* gene in the yeast chromosome
genetic reagent (include species here)				
cell line (include species here)				
transfected construct (include species here)				
biological sample (include species here)				
antibody	FIC1 (H-91) rabbit anti-ATP8B1 antibody	Santa-Cruz Biotechnology	Cat#sc-134967	(1/10000) This product has been discontinued
antibody	Goat anti-rabbit HRP-coupled IgG antibody	Biorad	Cat#1706515	1/2000

recombinant DNA reagent	ATP8B1 cDNA	Joost Holthuis laboratory	Uniprot: O43520	
recombinant DNA reagent	CDC50 cDNA	Joost Holthuis laboratory	Uniprot: Q9NV96	
sequence-based reagent				
peptide, recombinant protein	ATP8B1 C-terminal peptide	Biomatik Company		
peptide, recombinant protein	ATP8B1 phosphorylated C-terminal peptide	Biomatik Company		Phosphorylated on S1223
peptide, recombinant protein	HRV 3C protease	This study		
peptide, recombinant protein	TEV protease	This study		
commercial assay or kit	NucleoSpin Plasmid, Mini kit for Plasmid DNA	Macherey-Nagel	Cat#740588.250	
commercial assay or kit	QuickChange II XL site-directed mutagenesis kit	Agilent technologies	Cat#200521	
commercial assay or kit	Amicon 100 kDa cutoff	EMD Millipore	Cat#UFC510024	For volume ≤0.5 mL
commercial assay or kit	Vivaspin 500	Sartorius	Cat#VS0142	For volumes from 0.5 to 0.005 mL

commercial assay or kit	Vivaspin 6	Sartorius	Cat#VS0641	For volumes from 0.5 to 6 mL
commercial assay or kit	Vivaspin 20	Sartorius	Cat#VS2041	For volumes from 2 to 20 mL
commercial assay or kit	Superose 6 Increase 10/300 GL	GE Healthcare/ Cytiva	Cat#29091596	
commercial assay or kit	TSK3000-SW	Tosoh Bioscience	Cat#08541	
commercial assay or kit	Streptavidin -sepharose resin	GE Healthcare/ Cytiva	Cat#17511301	
chemical compound, drug	*n*-dodecyl-β-D-maltopyranoside, Anagrade	Anatrace	Cat#D310	
chemical compound, drug	Cholesteryl hemisuccinate	Sigma	Cat#C6013	
chemical compound, drug	Lauryl maltose neopentyl glycol	Anatrace	Cat#NG310	
chemical compound, drug	Sodium chloride	ROTH	Cat#3957.2	
chemical compound, drug	Potassium chloride	Sigma-Aldrich	Cat#P9541	
chemical compound, drug	Magnesium chloride	Sigma-Aldrich	Cat#M2670	

chemical compound, drug	MOPS	Sigma-Aldrich	Cat#M1254	
chemical compound, drug	ATP	Sigma-Aldrich	Cat#A2383	
chemical compound, drug	Phospho(enol)pyruvic acid	Sigma-Aldrich	Cat#860077	
chemical compound, drug	(β-nicotinamide adenine dinucleotide, reduced disodium salt hydrate (NADH) Grade I, disodium salt	Roche	Cat#10107730001	
chemical compound, drug	Glycerol	VWR Chemicals	Cat#24387.292	
chemical compound, drug	D-glucose	Becton Dickinson	Cat#215530	
chemical compound, drug	D-galactose	Sigma Aldrich	Cat#G5388	
chemical compound, drug	SIGMAFAST EDTA-free protease inhibitor cocktail	Sigma	Cat#S8830	
chemical compound, drug	Brain phosphatidylinositol-4-phosphate (PI4P)	Avanti Polar Lipids, Inc	Cat#840045P	

chemical compound, drug	Brain phosphatidylinositol-4,5-bisphosphate (PI(4,5)P_2)	Avanti Polar Lipids, Inc	Cat#840046P	
chemical compound, drug	1,2-dioleoyl-*sn*-glycero-3-phospho-(1'-myo-inositol-3'-phosphate) (PI(3)P)	Avanti Polar Lipids, Inc	Cat#850150P	
chemical compound, drug	1,2-dioleoyl-*sn*-glycero-3-phospho-(1'-myo-inositol-5'-phosphate) (PI(5)P)	Avanti Polar Lipids, Inc	Cat#850152P	
chemical compound, drug	1,2-dioleoyl-*sn*-glycero-3-phospho-(1'-myo-inositol-3',4'-bisphosphate) (PI(3,4)P_2)	Avanti Polar Lipids, Inc	Cat#850153P	
chemical compound, drug	1,2-dioleoyl-*sn*-glycero-3-phospho-(1'-myo-inositol-3',5'-bisphosphate) (PI(3,5)P_2)	Avanti Polar Lipids, Inc	Cat#850154P	
chemical compound, drug	1,2-dioleoyl-*sn*-glycero-3-phospho-(1'-myo-inositol-3',4',5'-trisphosphate) (PI(3,4,5)P_3)	Avanti Polar Lipids, Inc	Cat#850156P	
chemical compound, drug	Brain phosphatidylserine (PS)	Avanti Polar Lipids, Inc	Cat#840032P	

chemical compound, drug	1-palmitoyl-2-oleoyl-*sn*-glycero-3-phosphocholine (POPC)	Avanti Polar Lipids, Inc	Cat#850457P	
chemical compound, drug	1-palmitoyl-2-oleoyl-*sn*-glycero-3-phosphoethanolamine (POPE)	Avanti Polar Lipids, Inc	Cat#850757P	
chemical compound, drug	1-palmitoyl-2-oleoyl-*sn*-glycero-3-phosphoserine (POPS)	Avanti Polar Lipids, Inc	Cat#840034P	
chemical compound, drug	Bovine heart cardiolipin (CL)	Avanti Polar Lipids, Inc	Cat#840012P	
chemical compound, drug	egg chicken sphingomyelin (SM)	Avanti Polar Lipids, Inc	Cat#860061P	
chemical compound, drug	edelfosine	Avanti Polar Lipids, Inc	Cat#999995P	
chemical compound, drug	Miltefosine (Fos-Choline-16)	Anatrace	Cat#F316	
chemical compound, drug	1-stearoyl-2-hydroxy-sn-glycero-3-phosphocholine (Lyso-PC)	Sigma	Cat#L2131	
chemical compound, drug	Pyruvate kinase	Sigma	Cat#P7768	

chemical compound, drug	Lactate dehydrogenase	Sigma	Cat#L1006	
chemical compound, drug	[γ-^{32}P]ATP	Perkin-Elmer	Cat#BLU002A	
Chemical compound, drug	His-probe-HRP	Thermo Scientific	Cat#15165	
Software, algorithm	EPU v 2.3	Thermo Fisher	https://www.thermofisher.com/it/en/home/electron-microscopy/products/software-em-3d-vis/epu-software.html	
Software, algorithm	cryoSPARC v3	Punjani et al., 2017 Structura Biotechnology Inc.	https://www.nature.com/articles/nmeth.4169	
software, algorithm	ChimeraX 1.4	Goddard et al., 2018	https://www.cgl.ucsf.edu/chimerax/	
software, algorithm	I-TASSER	Yang et al., 2015	https://zhanggroup.org/I-TASSER/	
Software, algorithm	Coot 0.9.6	Emsley et al., 2010	https://doi.org/10.1107/S0907444904019158 https://www2.mrc-lmb.cam.ac.uk/personal/pemsley/coot/	
Software, algorithm	Phenix 1.19.2	Liebschner et al., 2019	https://doi.org/10.1107/S2059798318006551 http://phenix-online.org/	
Software, algorithm	Molprobity 4.5.1	Williams et al., 2018	https://doi.org/10.1002/pro.3330	

			http://molprobity.biochem.duke.edu	
software, algorithm	ImageJ	Schneider, C. A., Rasband, W. S., & Eliceiri, K. W. (2012). NIH Image to ImageJ: 25 years of image analysis. *Nature Methods*, *9*(7), 671–675. doi:10.1038/nmeth.2089	https://imagej.nih.gov/ij/	
software, algorithm	Prism 9	GraphPad	https://www.graphpad.com/scientific-software/prism/	
other	C-Flat 1.2/1.3 Cryo-EM Grid - Copper (400 Grid Mesh, 20nm Carbon Thickness)	Molecular Dimensions	CF-1.2/1.3-4CU-50	

621

622

623 **Materials**

624 Products for yeast and bacteria cultures were purchased from Difco (BD Biosciences) and Sigma.
625 DNA Polymerase, restriction and modification enzymes, as well as Endoglycosidase H-MBP, were
626 purchased from New England Biolabs (NEB). Lauryl Maltose Neopentyl Glycol (LMNG, NG310), *n*-
627 dodecyl-β-D-maltopyranoside (DDM, D310) and miltefosine (also known as Fos-choline-16, FC-16,
628 F316) were purchased from Anatrace. Cholesteryl hemisuccinate (CHS, C6013) and 1-stearoyl-2-
629 hydroxy-sn-glycero-3-phosphocholine (Lyso-PC) were purchased from Sigma. Brain
630 phosphatidylinositol-4-phosphate (PI(4)P), brain phosphatidylinositol-4,5-bisphosphate (PI(4,5)P_2),
631 1,2-dioleoyl-*sn*-glycero-3-phospho-(1'-myo-inositol-3'-phosphate) (PI(3)P), 1,2-dioleoyl-*sn*-glycero-
632 3-phospho-(1'-myo-inositol-5'-phosphate) (PI(5)P), 1,2-dioleoyl-*sn*-glycero-3-phospho-(1'-myo-
633 inositol-3',4'-bisphosphate) (PI(3,4)P_2), 1,2-dioleoyl-*sn*-glycero-3-phospho-(1'-myo-inositol-3',5'-
634 bisphosphate) (PI(3,5)P_2), 1,2-dioleoyl-*sn*-glycero-3-phospho-(1'-myo-inositol-3',4',5'-trisphosphate)

635 (PI(3,4,5)P_3), brain phosphatidylserine (PS), 1-palmitoyl-2-oleoyl-*sn*-glycero-3-phosphocholine
636 (POPC), 1-palmitoyl-2-oleoyl-*sn*-glycero-3-phosphoethanolamine (POPE), 1-palmitoyl-2-oleoyl-*sn*-
637 glycero-3-phosphoserine (POPS), heart cardiolipin (CL), egg sphingomyelin (SM) and edelfosine
638 were purchased from Avanti Polar lipids. The ATP8B1 C-terminal peptide
639 RRSAYAFSHQRGYADLISSGRSIRKKRSPLDAIVADGTAEYRRTGDS, encompassing residues
640 1205-1251, and its S1223 phosphorylated derivative, were ordered from Biomatik Company
641 (Biomatik, Ontario, Canada). Both peptides were resuspended at 1 mM in 50 mM MOPS-Tris pH 7,
642 100 mM KCl, 1 mM dithiothreitol (DTT). ATP8B1 was detected using a mouse anti-ATP8B1 antibody
643 from Santa Cruz Biotechnology (Epitope: 1161-1251, ref: SC-134967, no longer available). An anti-
644 rabbit HRP-coupled antibody (1706515) was purchased from Biorad. His-tagged CDC50A was
645 detected using a His-probe™ -HRP from Thermo Scientific (15165). Precast stain-free gradient gels
646 for tryptophan fluorescence (4568084) as well as Precision Plus Protein Standards (1610393) were
647 purchased from Biorad. Pyruvate kinase (P7768), lactate dehydrogenase (L1006), and an EDTA-
648 free protease inhibitor cocktail (S8830) were purchased from Sigma. [γ-^{32}P]ATP was purchased from
649 Perkin-Elmer (BLU002A). Streptavidin-sepharose resin was purchased from GE/Cytiva (17511301).
650 The pig kidney $\alpha1\beta1$ isoform of Na^+/K^+-ATPase was a kind gift from Natalya U. Fedosova, and
651 microsomal membranes were prepared as previously described (Klodos et al., 2002).
652
653 **Yeast strains and plasmids**
654 The *Saccharomyces cerevisiae* W303.1b/*Δpep4* (*MATα, leu2-3, his3-11, ura3-1, ade2-1, Δpep4,*
655 *can^r, cir$^+$*) yeast strain was used for co-expression of ATP8B1 and CDC50A. The cDNAs encoding
656 human ATP8B1 (hATP8B1, Uniprot: O43520; A1154T natural variant) and human CDC50A
657 (hCDC50A, Uniprot: Q9NV96) were a kind gift from Joost Holthuis (University of Osnabruck,
658 Germany). hATP8B1 was supplemented at its 5' end with a sequence coding a biotin acceptor
659 domain (BAD), and a sequence coding a TEV protease cleavage site. The cleavage site was flanked
660 by 2 glycines toward BAD and 4 glycines toward hATP8B1. Similarly, a sequence coding a
661 decahistidine tag was added at the 5' end of hCDC50A. The tagged genes were cloned in a unique
662 co-expression pYeDP60 plasmid (Jacquot et al., 2012). In this vector, hATP8B1 and hCDC50A are
663 both placed under the control of a strong galactose-inducible promoter, *GAL10/CYC1*. The D454N
664 mutation was introduced by site-directed mutagenesis using the QuickChange™ II XL site-directed
665 mutagenesis kit (Agilent technologies). An overlap extension PCR strategy was used to insert the
666 3C protease site (LEVLFQGP) between Pro42 and Glu43 and/or between Glu1174 and Ser1175.
667 Primers and plasmids used in this study are listed in ***Tables 3 and 4***.
668

Primers	
FwBad ATP8B1	5'- ACAGTTTAAACGGTGGTGAGAATCTTTATTTTCAGGGCGGTGGTGGTGGTATGAGTACAG AAAGAGACTCAG - 3'
RevBad ATP8B1	5'- AGCATGGAGCTCTCAGCTGTCCCCGGTGCGCCTGTA - 3'
FwHis CDC50A	5' – CACAGAATTCTAGTATGCATCATCATCATCATCATCATCATCACCTAGGTGGTATGGC GATGAACTATAACGCG – 3'
RevHis CDC50A	5' – CACAGAGCTCCTAAATGGTAATGTCAGCTGTATTAC - 3'
Fwd D454N	5'- GATCCATTATATCTTCTCTAATAAGACGGGGACACTCACAC -3'
Rev D454N	5'- GTGTGAGTGTCCCCGTCTTATTAGAGAAGATATAATGGATC -3'
Fwd 3C-P43	5' – CTGGAGGTGCTGTTCCAGGGCCCGGAACAAAACCGAGTCAACAGGGAAGC – 3'
Rev 3C-P43	5' – CGGGCCCTGGAACAGCACCTCCAGTGGTTCAACAGCAGACCCCTGGTCATCAAG – 3'
Fwd 3C-E1174	5' – CTGGAGGTGCTGTTCCAGGGCCCGAGTGATAAGATCCAGAAGCATC – 3'
Rev 3C-E1174	5' – CGGGCCCTGGAACAGCACCTCCAGTTCTGATGGCCAGATGGTCAT– 3'

669

670 **Table 3: Primers used in this study.**

671

672

Plasmids	References
pYeDP60_BAD-TevS-ATP8B1 (WT) / His_{10}CDC50A	This study
pYeDP60_BAD-TevS-ATP8B1 (D454N) / His_{10}CDC50A	This study
pYeDP60_BAD-TevS-ATP8B1 (P42-3CS) / His_{10}CDC50A	This study
pYeDP60_BAD-TevS-ATP8B1 (P42-3CS) / His_{10}CDC50A	This study
pYeDP60_BAD-TevS-ATP8B1 (E1174-3CS) / His_{10}CDC50A	This study
pYeDP60_BAD-TevS-ATP8B1 (P43+E1174-3CS) / His_{10}CDC50A	This study
pRK793 MBP-Tev_{site}-His_7-TEV_{S219V}-Arg_5	(Kapust et al., 2001)
pGEX-4T-2 His_6-Arg_8-GST-3C	

673

674 **Table 4: Plasmids used in this study.**

675

676

677 **Co-expression of ATP8B1 with CDC50A in yeast membranes**

678 Yeasts were transformed using the lithium-acetate method (68). Yeast cultures, recombinant protein
679 expression and membrane preparation were performed as described previously (45, 69). Briefly,
680 yeast growth took place in a glucose-containing rich growth medium supplemented with 2.7%

681 ethanol at 28°C for 36 h, whereas expression of the proteins of interest took place during an
682 additional 18 h in the presence of 2% galactose, at 18°C. Yeast cells were harvested by
683 centrifugation, washed first with ice-cold ddH_2O, then with ice-cold TEKS buffer (50 mM Tris-HCl pH
684 7.5, 1 mM EDTA, 0.1 M KCl, 0.6 M sorbitol), and finally resupended in TES buffer (50 mM Tris-HCl
685 pH 7.5, 1 mM EDTA, 0.6 M sorbitol) supplemented with protease inhibitors. The cells were
686 subsequently broken with 0.5 mm glass beads using a "Pulverisette 6" planetary mill (Fritsch). The
687 crude extract was then spun down at 1,000 *g* for 20 min at 4°C, to remove cell debris and nuclei.
688 The resulting supernatant was centrifuged at 20,000 *g* for 20 min at 4°C, yielding S2 supernatant
689 and P2 pellet. The S2 supernatant was further centrifuged at 125,000 *g* for 1 h at 4°C. The resulting
690 P2 and P3 pellets were finally resuspended at about 30-50 mg ml^{-1} of total protein in TES buffer. P2
691 and P3 membrane fractions were pooled and the ATP8B1 content was estimated, by
692 immunoblotting, to be about 0.5% of total proteins.
693
694 **Purification of the ATP8B1-CDC50A complex**
695 Membranes obtained after co-expression of ATP8B1 and CDC50A (P2+P3) were diluted to 5 mg ml^{-}
696 ^{1} of total protein in ice-cold buffer A (50 mM MOPS-Tris at pH 7, 100 mM NaCl, 1 mM DTT, 20%
697 (w/v) glycerol and 5 mM $MgCl_2$), supplemented with 1 mM PMSF and an EDTA-free protease
698 inhibitor mixture. The suspension was stirred gently on a wheel for 5 min at 4°C. Washed membranes
699 were pelleted by centrifugation at 100,000 *g* for 1 h at 4°C. For cryo-EM sample preparation, this
700 step was omitted and the membranes were directly incubated with DDM as follows. The pelleted
701 membranes were resuspended at 5 mg ml^{-1} of total protein in ice-cold buffer A supplemented with 1
702 mM PMSF and the EDTA-free protease inhibitor mixture. A mixture of DDM and CHS at final
703 concentrations of 15 mg ml^{-1} and 3 mg ml^{-1}, respectively, was added, resulting in a DDM/protein ratio
704 of 3/1 (w/w). The suspension was then stirred gently on a wheel for 1 h at 4°C. Insoluble material
705 was pelleted by centrifugation at 100,000 *g* for 1 h at 4°C. The supernatant, containing solubilized
706 proteins, was applied onto a streptavidin-sepharose resin and incubated for 2 h at 6°C to allow
707 binding of the BAD-tagged ATP8B1 to the resin.
708 For structural studies the DDM/CHS mixture was exchanged to LMNG/CHS. The resin was washed
709 twice with three resin volumes of ice-cold buffer B (50 mM MOPS-Tris at pH 7, 100 mM KCl, 1 mM
710 DTT, 20% (w/v) glycerol and 5 mM $MgCl_2$), supplemented with 0.2 mg ml^{-1} LMNG and 0.02 mg ml^{-1}
711 CHS in the presence of 1 mM PMSF and an EDTA-free protease inhibitor cocktail. The resin was
712 then washed thrice with three resin volumes of ice-cold buffer B supplemented with 0.1 mg ml^{-1}
713 LMNG and 0.01 mg ml^{-1} CHS. Elution was performed by addition of 60 μg of purified TEV per ml of
714 resin and overnight incubation at 6°C. The eluted fraction was concentrated using a Vivaspin unit
715 (100 kDa MWCO) prior to injection on a size-exclusion Superose 6 10/300GL increase column

716 equilibrated with buffer C (50 mM MOPS-Tris pH 7, 100 mM KCl, 1 mM DTT, 5 mM $MgCl_2$, 0.03 mg
717 ml^{-1} LMNG and 0.003 mg ml^{-1} CHS). This step allowed separation of the TEV protease from the
718 ATP8B1-CDC50A complex. The ATP8B1-CDC50A-containing fractions were pooled, concentrated
719 using a Vivaspin unit (50 kDa MWCO) to concentrate the protein and the detergent micelles, and
720 supplemented with LMNG and PI(3,4,5)P_3 to final concentrations of 0.35 mg ml^{-1} and 0.05 mg ml^{-1},
721 respectively (PI(3,4,5)P_3/LMNG ratio of 0.15). The sample was then incubated for 1 h at room
722 temperature and overnight at 6°C to allow lipid diffusion prior injection on a Superose 6 10/300GL
723 increase column equilibrated with buffer C, to remove the excess of detergent/lipid micelles.
724 For functional studies, the resin was washed four times with three resin volumes of ice-cold buffer B
725 supplemented with 0.5 mg ml^{-1} DDM and 0.1 mg ml^{-1} CHS in the presence of 1 mM PMSF and an
726 EDTA-free protease inhibitor cocktail. Elution was performed by addition of 60 μg of purified TEV
727 per mL of resin by overnight incubation at 6°C. For purifying the 3C protease site-containing version
728 of ATP8B1, 240 μg of purified 3C protease per ml of resin were added together with the TEV
729 protease. Purified ATP8B1-CDC50A complex was snap-frozen and stored at -80°C. ATP8B1 protein
730 concentrations were calculated based on Coomassie-blue staining of SDS-PAGE gels using known
731 amounts of purified Drs2.
732
733 **Grid preparation for cryo-EM**
734 The ATP8B1-CDC50A complex at a concentration of 0.8 mg ml^{-1} was supplemented with 1 mM
735 $BeSO_4$ and 5 mM KF to stabilize an E2-BeF_x form mimicking the E2P conformation. The sample was
736 incubated on ice for 1 h and 3 μl were added to freshly glow-discharged (45 s at 15 mA) C-flat Holey
737 Carbon grids, CF-1.2/1.3-4C (Protochips), which were subsequently vitrified at 4°C and 100%
738 humidity for 4.5 s with a blotting force of -1 on a Vitrobot IV (Thermo Fisher Scientific) with standard
739 Vitrobot filter paper (ø55/20 mm, Grade 595).
740
741 **Cryo-EM data collection**
742 The Data were collected on a Titan Krios G3i (EMBION Danish National cryo-EM Facility – Aarhus
743 node) with X-FEG operated at 300 kV and equipped with a Gatan K3 camera and a Bioquantum
744 energy filter using a slit width of 20 eV and with 30° tilt. Movies were collected using aberration-free
745 image shift data collection (AFIS) in EPU (Thermo Fisher Scientific) as 1.5-s exposures in super-
746 resolution mode at a physical pixel size of 0.66 Å/pixel (magnification of 130,000x) with a total
747 electron dose of 60 $e^-/Å^2$. A total of 3941 movies were collected.
748
749 **Cryo-EM data processing**

750 Processing was performed in cryoSPARC v3 (Punjani et al., 2017). Patch Motion Correction and
751 Patch CTF were performed before low-quality micrographs (e.g. micrographs with crystalline ice,
752 high motion) were discarded. Particles were initially picked using a circular blob on ~1000
753 micrographs. These were aligned in 2D to produce references for template picking on all movies.
754 Particles were extracted in a 416-pixel box and Fourier cropped to a 104-pixel box (2.64 Å/pixel). *Ab*
755 *initio* references were produced using a subset of all particles. One protein-like reference and
756 multiple junk references were used in multiple rounds of heterogeneous refinement. Selected
757 particles were then re-extracted in a 416-pixel box (0.66 Å/pixel) before non-uniform (NU) refinement
758 (Punjani et al., 2020). The particle stack was then CTF-refined using Local CTF refinement and
759 motion-corrected using Local motion correction before final non-uniform (NU) refinement. Data
760 processing flow-chart is available in ***Figure 2 – figure supplement 1***.
761
762 **Model building**
763 The ATP8B1-CDC50A model was built using a homology model of ATP8B1 generated by I-TASSER
764 (Yang et al., 2015) with Drs2 $E2P_{autoinhibited}$ (PDB: 6ROH) and from the CDC50A structure of the
765 ATP8A1-CDC50A complex in E2P (PDB: 6K7L) as templates. The cryo-EM map was sharpened
766 with a B factor of -84 $Å^2$ using the Autosharpen tool in PHENIX (Terwilliger et al., 2018).
767 The model was manually generated and relevant ligands added with COOT (Emsley et al., 2010)
768 before real space refinement in PHENIX (Afonine et al., 2018) with secondary structure restraints.
769 Model validation was performed using MolProbity (Chen et al., 2010) in PHENIX (Adams et al.,
770 2010), and relevant metrics are listed in ***Supplementary file 1***. Representative map densities with
771 fitted models can be seen in ***Figure 2 – figure supplement 2***. Figures were prepared in ChimeraX
772 (Pettersen et al., 2021).
773
774 **Endoglycosidase treatment**
775 For CDC50A deglycosylation, the purified sample was treated with EndoH-MBP according to
776 manufacturer instructions. Briefly, about 1.5 μg of purified ATP8B1-CDC50A complex was
777 denatured for 3 min at 96°C in the presence of 0.5% SDS and 40 mM DTT, in a final volume of 19.5
778 μl. The denatured proteins were then supplemented with 500 U of EndoH-MBP (EndoHf, NEB) and
779 incubated for 45 min at 37°C. Then 20 μl of urea-containing Laemmli denaturation buffer were added
780 and the samples were incubated for 10 min at 30°C prior loading on an 8% SDS-PAGE.
781
782 **Determination of subunit stoichiometry**
783 About 6.5 μg of purified ATP8B1-CDC50A complex was denatured for 5 min at 96°C, in the presence
784 of 0.5% SDS and 40 mM DTT and in a final volume of 250 μl. The denatured proteins were then

785 supplemented with 750 U of EndoH-MBP and incubated for 1 h at 37°C. Samples were then
786 precipitated by adding 1 volume of 1 M trichloroacetic acid (TCA). After 45 min on ice, samples were
787 centrifuged at 20,000 *g* for 25 min at 4°C. Supernatant was discarded and samples were centrifuged
788 again at 20,000 *g* for 5 min at 4°C to remove traces of TCA. Pellets were then resuspended in 60 μl
789 urea-containing Laemmli buffer (50 mM Tris-HCl pH 6.8, 0.7 M β-mercaptoethanol, 2.5% w/v SDS,
790 0.5 mM EDTA, 4.5 M urea, 0.005% w/v bromophenol blue). Thirty μl of each sample (about 3.25 μg
791 of purified complex) were loaded on a 4-15% gradient TGX™ stain-free gel. After 90 min
792 electrophoretic separation at 150 V and 40 mA, the gel was soaked in 5% (w/v) TCA for 10 min and
793 rinsed 3 times in ddH_2O. The gel was then exposed to UV (254 nm) for 5 min and images were
794 collected after 20 s of exposure. The relative intensity of ATP8B1 and CDC50A was quantified from
795 various amounts loaded onto gradient TGX™ stain-free gels using the ImageJ software.
796
797 **Phosphorylation of ATP8B1-CDC50A by [γ-^{32}P]ATP**
798 To study phosphorylation of the ATP8B1-CDC50A complex, about 0.5 μg of purified complex were
799 supplemented with [γ-^{32}P]ATP at a final concentration of 2 μM (5 mCi μmol^{-1}) and incubated at 0°C
800 in buffer B supplemented with 0.5 mg ml^{-1} DDM and 0.1 mg ml^{-1} CHS. Phosphorylation was stopped
801 after 30 s by addition of 1 sample volume of 1 M TCA, 5 mM H_3PO_4. Samples were then left for 40
802 min on ice for aggregation and 2 volumes of 0.5 M TCA in 2.5 mM H_3PO_4 were subsequently added
803 to help aggregation. Proteins were then centrifuged at 14,000 *g* for 25 min at 4°C. The supernatant
804 was removed, and the pellet was washed by addition of 0.5 M TCA in 0.5 mM H_3PO_4. Samples were
805 centrifuged again at 14,000 *g* for 25 min at 4°C. Supernatants were discarded, samples were
806 centrifuged again at 14,000 *g* for 5 min at 4°C to remove residual TCA. Pellets were then
807 resuspended at 4°C in 25 μl urea-containing Laemmli denaturation buffer. After resuspension, 15 μl
808 of each sample (about 0.3 μg of purified complex) were loaded on acidic gels. The stacking gel
809 contained 4% acrylamide, 65 mM Tris-H_3PO_4 pH 5.5, 0.1% SDS, 0.4% ammonium persulfate, and
810 0.2% TEMED, and the separating gel was a continuous 7% gel containing 65 mM Tris-H_3PO_4 pH
811 6.5, 0.1% SDS, 0.4% ammonium persulfate, and 0.05% TEMED. The gel tanks were immersed in a
812 water/ice bath and the pre-cooled running buffer contained 0.1% SDS and 170 mM MOPS-Tris at
813 pH 6.0. Dried gels were subsequently stained with Coomassie Blue before radioactivity was
814 measured, using a PhosphorImager equipment (Amersham Typhoon RGB, GE Healthcare).
815
816 **ATPase activity of purified ATP8B1-CDC50A**
817 For the ATP8B1-CDC50A complex, the rate of ATP hydrolysis was monitored continuously on an
818 Agilent 8453 diode-array spectrophotometer, using an enzyme-coupled assay. ATPase activity was
819 measured at either 30°C or 37°C in buffer B supplemented with 1 mM ATP, 1 mM

820 phosphoenolpyruvate, 0.4 mg ml^{-1} pyruvate kinase, 0.1 mg ml^{-1} lactate dehydrogenase, 250 μM
821 NADH, 1 mM NaN_3, 1 mg ml^{-1} DDM (2 mM), and residual CHS at 0.01 mg ml^{-1}. In these experiments,
822 50-200 μl of the purified ATP8B1-CDC50A complex (final concentrations of 1-5 μg ml^{-1}) was added
823 to a total volume of 1.8 ml. For measurement of the half-maximum inhibitory concentration (IC_{50}),
824 successive additions of the C-terminal peptide or its phosphorylated derivative (from a 1 mM stock
825 solution) to purified ATP8B1-CDC50A incubated in 43 μg ml^{-1} POPC (~ 57 μM), 25 μg ml^{-1} PI(4,5)P_2
826 (~ 23 μM) and 0.5 mg ml^{-1} DDM (~ 1 mM) in the assay cuvette were performed. Similarly, to
827 determine the maximum rate of ATP hydrolysis (V_{max}) and the apparent affinity (K_m) for PPIns,
828 successive additions of DDM and POPC to purified ATP8B1-CDC50A preincubated with 43 μg ml^{-1}
829 POPC, 25 μg ml^{-1} PI(4,5)P_2 and 0.5 mg ml^{-1} DDM were performed, in order to gradually decrease
830 the PIP/DDM ratio (while the POPC/DDM ratio remained constant). Conversion from NADH
831 oxidation rates expressed in mAU s^{-1} to ATPase activities expressed in μmol min^{-1} mg^{-1} was based
832 on the extinction coefficient of NADH at 340 nm (~ 6.2 mM^{-1} cm^{-1}). For all experiments,
833 photobleaching of NADH was reduced by inserting an MTO J310A filter that eliminates short
834 wavelength UV excitation light. This setup reduced the spontaneous rate of NADH absorption
835 changes down to ~ 0.01 mAU s^{-1}. ATPase activities measured for truncated ΔC1174 and
836 ΔN42/C1174 come from two independent purification batches, with similar results, and referred to
837 as 'purification #1' and 'purification #2' in the legend to figures.
838
839 **Quantification of n-dodecyl-β-D-maltoside bound to the transmembrane domain of purified**
840 **Drs2-Cdc50**
841 The yeast Drs2-Cdc50 flippase complex was purified by streptavidin-affinity chromatography, as
842 previously described (Azouaoui et al., 2017). The complex was eluted in a buffer containing 50 mM
843 MOPS-Tris pH 7, 100 mM KCl and 5 mM $MgCl_2$, supplemented with 0.5 mg ml^{-1} DDM, and
844 concentrated to about 1 mg ml^{-1} on YM100 Centricon units (Millipore). Next, the eluted complex was
845 supplemented with radioactive detergent (^{14}C-DDM, Commissariat à l'Énergie Atomique et aux
846 Énergies Alternatives, Saclay) as a tracer, in order to evaluate the amount of DDM bound to the
847 complex. A TSK3000 SW column (Tosoh Bioscience, Germany) was first equilibrated with 1 volume
848 of 50 mM MOPS-Tris pH 7, 100 mM KCl, 5 mM $MgCl_2$ supplemented with 0.5 mg ml^{-1} DDM, at room
849 temperature. A second volume of mobile phase was applied, now supplemented with ^{14}C-DDM. Both
850 the purified complex and the mobile phase contained ^{14}C-DDM to reach a specific activity of about
851 3.10^{-5} μCi per nmol of DDM. Fractions of 250 μl eluting between 5 ml and 10 ml were collected.
852 Protein and ^{14}C-DDM contents were determined by the bicinchoninic assay and liquid scintillation,
853 respectively.
854

855 **HRV 3C protease purification**

856 *Escherichia coli* (BL21) cells transformed with a His_6-Arg_8-GST-3C protease coding sequence
857 cloned into pGEX-4T-2 plasmid were cultured in LB medium containing 100 μg L^{-1} ampicillin and 30
858 μg L^{-1} chloramphenicol. Protein expression was induced with 0.2 mM isopropyl-β-D-1-
859 thiogalactopyranoside for 16 h at 18°C. Cells were harvested and lysed in lysis buffer C (50 mM
860 NaH_2PO_4 pH 8, 500 mM NaCl, 30 mM imidazole, 10% glycerol (v/v) and 5 mM β-mercaptoethanol)
861 by sonication. Cell debris were removed by centrifugation at 15,000 *g* for 30 min at 4°C. The clarified
862 lysate was loaded onto a HisTrap FF crude column (GE). To remove impurities, the column was
863 washed with 6 column volumes of lysis buffer C followed by 15 column volumes of washing buffer D
864 (50 mM NaH_2PO_4 pH 8, 150 mM NaCl, 30 mM imidazole, and 5 mM β-mercaptoethanol). The protein
865 of interest was eluted with a gradient of elution buffer E (50 mM NaH_2PO_4 pH 8, 150 mM NaCl, 500
866 mM imidazole, and 5 mM β-mercaptoethanol). Fractions of interest were diluted two-fold and loaded
867 onto a GST-Trap HP column. To remove impurities, the column was washed with 10 column volumes
868 of GST-washing buffer F (8 mM Na_2HPO_4, 1.5 mM KH_2PO_4 pH 7.2, 140 mM NaCl, 2.7 mM KCl, 0.1
869 mM EDTA, 1 mM DTT). The protein of interest was eluted with a gradient of GST-washing buffer F
870 supplemented with 40 mM of reduced glutathione. The fraction of interest was directly loaded onto
871 a SP Sepharose Fast-Flow HiTrap column pre-equilibrated in buffer G (50 mM NaH_2PO_4 pH 8, 100
872 mM NaCl, 0.1 mM EDTA and 1 mM DTT). The column was washed with 5 column volumes of buffer
873 D and the protein of interest was eluted with a gradient of buffer H (50 mM NaH_2PO_4 pH 8, 1.5 M
874 NaCl, 0.1 mM EDTA and 1 mM DTT). Fractions containing the protein of interest were loaded on a
875 HiLoad 16/600 Superdex 200 column pre-equilibrated in buffer I (50 mM MOPS-Tris pH 7, 100 mM
876 KCl, 20% (w/v) glycerol and 1 mM DTT). Fractions containing the 3C protease were pooled,
877 concentrated to 3 mg ml^{-1}, aliquoted, snap-frozen and stored at -80°C.

878

879 **TEV protease purification**

880 *Escherichia coli* C43 (DE3) cells transformed with a MBP-TEV_{site}-His_7-TEV_{S219V}-Arg_5 protease coding
881 sequence cloned into the pRK793 plasmid were cultured in LB medium containing 100 μg L^{-1}
882 ampicillin. Protein expression was induced with 0.5 mM isopropyl-β-D-1-thiogalactopyranoside for
883 16 h at 18°C. Cells were harvested and lysed in lysis buffer J (50 mM Tris-HCl pH 7.5, 300 mM NaCl,
884 10% v/v glycerol) by sonication. Cell debris were removed by centrifugation at 10,000 *g* for 20 min
885 at 4°C. The clarified lysate was loaded onto a HisTrap FF crude column (GE). To remove impurities,
886 the column was washed with 6 column volumes of lysis buffer J followed by 25 column volumes of
887 washing buffer K (50 mM Tris-HCl pH 7.5, 300 mM NaCl, 10% v/v glycerol v/v, 25 mM imidazole).
888 The protein of interest was eluted with a gradient of elution buffer L (50 mM Tris-HCl pH 7.5, 300
889 mM NaCl, 10% v/v Glycerol, 500 mM imidazole). Fractions of interest were diluted three-fold in buffer

890 M (50 mM KH_2PO_4 pH 8, 0.1 mM EDTA and 1 mM DTT) and loaded to a SP Sepharose Fast-Flow
891 HiTrap column pre-equilibrated in buffer N (50 mM KH_2PO_4 pH 8, 100 mM NaCl, 0.1 mM EDTA and
892 1 mM DTT). The column was washed with 10 column volumes of buffer N. The protein of interest
893 was eluted with a gradient of buffer O (50 mM KH_2PO_4 pH 8, 1.5 M NaCl, 0.1 mM EDTA and 1 mM
894 DTT). Fractions containing the protein of interest were loaded on a HiLoad 16/600 Superdex 200
895 column pre-equilibrated in buffer P (50 mM Tris-HCl pH 7.5, 200 mM NaCl). Elution fractions
896 containing the TEV protease were pooled, supplemented with 30% glycerol (v/v), concentrated to 1
897 mg ml^{-1}, aliquoted, snap-frozen and stored at -80°C.
898
899 **Statistical analysis, curve fitting and equation used in this study**
900 Statistical analysis and curve fitting was carried out with the GraphPad Prism 9 software, and
901 statistical significance was assigned to differences with a p value of <0.05.
902 GraphPad Prism log (inhibitor) vs response-variable slope (four parameters) non-linear regression
903 analysis was used to fit data displayed in Figure 5B, 5C and Figure 4 – figure supplement 2B. This
904 non-linear regression model is given by:
905 Y = Bottom+(Top-Bottom)/(1+10^((LogIC50 – X)*HillSlope)), where Y is the expected response, Top
906 and Bottom are plateaus in the unit of the Y axis, IC50 is the concentration of peptide (or BeFx for
907 Figure 4 – figure supplement 2B) that gives a response halfway between Top and Bottom, and
908 HillSlope is the slope at the steepest part of the curve, also known as the Hill slope.
909 GraphPad Prism Michaelis-Menten non-linear regression analysis was used to fit data displayed in
910 Figure 6C and Figure 4 – figure supplement 2C. This non-linear regression model is given by:
911 Y = Vmax*X/(Km+X), where Vmax is the maximum velocity in the same unit as Y and Km is the
912 Michaelis-Menten constant, in the same units as X. Km is the substrate concentration needed to
913 achieve a half-maximum enzyme velocity.
914
915

Acknowledgments

We thank Thomas Boesen, Andreas Bøggild and Taner Drace for technical support during EM data collection at the EMBION Danish National cryo-EM facility of Aarhus University (5072-00025B, Danish Agency for Research and Higher Education), Jesper Lykkegaard Karlsen for scientific computing support, Joost Holthuis (University of Osnabruck, Germany) for kindly providing the ATP8B1 and CDC50A cDNAs, Rosa López-Marqués (University of Copenhagen, Denmark) for the gift of the *S. cerevisiae Δpep4* strain and Mads Eriksen Christensen and Natalya Fedosova for generously providing the pig kidney α1β1 isoform of Na^+/K^+-ATPase. We also wish to thank David Stokes for critical reading of the manuscript and Philippe Champeil, Alenka Čopič, Guillaume Drin, Rasmus Kock Flygaard, Francis Haraux, Anaïs Lamy, José Luis Vázquez-Ibar and Marc le Maire for discussion and advice. Support for this work was provided by an ANR grant (ANR-14-CE09-0022) to G.L., by an EMBO short-term fellowship (7881), a PhD fellowship from the French ministry for higher education, research and innovation, and a Marie-Curie Individual Fellowship (LivFlip, grant agreement 101024542, H2020-MSCA-IF-2020) to T.D., by the French Infrastructure for Integrated Structural Biology (FRISBI; ANR-10-INSB-05), by the Centre National de la Recherche Scientifique (CNRS), by a professorship grant from the Lundbeck Foundation to P.N. (R310-2018-3713) and by the German Research Foundation (GU 1133/11-1) to T.G.P.

Data availability

The ATP8B1-CDC50A $E2P_{autoinhibited}$ cryo-EM map described in this article has been deposited in the Electron Microscopy Data Bank (EMDB) (accession number: EMD-13711) and the atomic model has been deposited in the Protein Data Bank (PDB) (accession number: 7PY4).

945 **References**

946

947 Adams PD, Afonine PV, Bunkóczi G, Chen VB, Davis IW, Echols N, Headd JJ, Hung L-W, Kapral
948 GJ, Grosse-Kunstleve RW, McCoy AJ, Moriarty NW, Oeffner R, Read RJ, Richardson DC,
949 Richardson JS, Terwilliger TC, Zwart PH. 2010. PHENIX: a comprehensive Python-based system
950 for macromolecular structure solution. *Acta Crystallogr D Biol Crystallogr* **66**:213–221.
951 doi:10.1107/S0907444909052925

952 Afonine PV, Poon BK, Read RJ, Sobolev OV, Terwilliger TC, Urzhumtsev A, Adams PD. 2018. Real-
953 space refinement in PHENIX for cryo-EM and crystallography. *Acta Crystallogr Sect Struct Biol*
954 **74**:531–544. doi:10.1107/S2059798318006551

955 Albers RW. 1967. Biochemical aspects of active transport. *Annu Rev Biochem* **36**:727–756.
956 doi:10.1146/annurev.bi.36.070167.003455

957 Andersen JP, Vestergaard AL, Mikkelsen SA, Mogensen LS, Chalat M, Molday RS. 2016. P4-
958 ATPases as Phospholipid Flippases-Structure, Function, and Enigmas. *Front Physiol* **7**:275.
959 doi:10.3389/fphys.2016.00275

960 Azouaoui H, Montigny C, Dieudonné T, Champeil P, Jacquot A, Vázquez-Ibar JL, Le Maréchal P,
961 Ulstrup J, Ash M-R, Lyons JA, Nissen P, Lenoir G. 2017. High phosphatidylinositol 4-phosphate
962 (PI4P)-dependent ATPase activity for the Drs2p-Cdc50p flippase after removal of its N- and C-
963 terminal extensions. *J Biol Chem* **292**:7954–7970. doi:10.1074/jbc.M116.751487

964 Bai L, Kovach A, You Q, Hsu H-C, Zhao G, Li H. 2019. Autoinhibition and activation mechanisms of
965 the eukaryotic lipid flippase Drs2p-Cdc50p. *Nat Commun* **10**:4142. doi:10.1038/s41467-019-12191-
966 9

967 Bai L, You Q, Jain BK, Duan HD, Kovach A, Graham TR, Li H. 2020. Transport mechanism of P4
968 ATPase phosphatidylcholine flippases. *eLife* **9**:e62163. doi:10.7554/eLife.62163

969 Balla T. 2013. Phosphoinositides: tiny lipids with giant impact on cell regulation. *Physiol Rev*
970 **93**:1019–1137. doi:10.1152/physrev.00028.2012

971 Bohdanowicz M, Grinstein S. 2013. Role of phospholipids in endocytosis, phagocytosis, and
972 macropinocytosis. *Physiol Rev* **93**:69–106. doi:10.1152/physrev.00002.2012

973 Bretscher MS. 1972. Asymmetrical lipid bilayer structure for biological membranes. *Nature New Biol*
974 **236**:11–12. doi:10.1038/newbio236011a0

975 Bryde S, Hennrich H, Verhulst PM, Devaux PF, Lenoir G, Holthuis JCM. 2010. CDC50 proteins are
976 critical components of the human class-1 P4-ATPase transport machinery. *J Biol Chem* **285**:40562–
977 40572. doi:10.1074/jbc.M110.139543

978 Bull LN, van Eijk MJ, Pawlikowska L, DeYoung JA, Juijn JA, Liao M, Klomp LW, Lomri N, Berger R,
979 Scharschmidt BF, Knisely AS, Houwen RH, Freimer NB. 1998. A gene encoding a P-type ATPase

980 mutated in two forms of hereditary cholestasis. *Nat Genet* **18**:219–224. doi:10.1038/ng0398-219
981 Chalat M, Moleschi K, Molday RS. 2017. C-terminus of the P4-ATPase ATP8A2 functions in protein
982 folding and regulation of phospholipid flippase activity. *Mol Biol Cell* **28**:452–462.
983 doi:10.1091/mbc.E16-06-0453
984 Chaptal V, Delolme F, Kilburg A, Magnard S, Montigny C, Picard M, Prier C, Monticelli L, Bornert O,
985 Agez M, Ravaud S, Orelle C, Wagner R, Jawhari A, Broutin I, Pebay-Peyroula E, Jault J-M, Kaback
986 HR, le Maire M, Falson P. 2017. Quantification of Detergents Complexed with Membrane Proteins.
987 *Sci Rep* **7**:41751. doi:10.1038/srep41751
988 Chen VB, Arendall WB, Headd JJ, Keedy DA, Immormino RM, Kapral GJ, Murray LW, Richardson
989 JS, Richardson DC. 2010. MolProbity: all-atom structure validation for macromolecular
990 crystallography. *Acta Crystallogr D Biol Crystallogr* **66**:12–21. doi:10.1107/S0907444909042073
991 Clark J, Anderson KE, Juvin V, Smith TS, Karpe F, Wakelam MJO, Stephens LR, Hawkins PT. 2011.
992 Quantification of PtdInsP3 molecular species in cells and tissues by mass spectrometry. *Nat*
993 *Methods* **8**:267–272. doi:10.1038/nmeth.1564
994 Coleman JA, Kwok MCM, Molday RS. 2009. Localization, purification, and functional reconstitution
995 of the P4-ATPase Atp8a2, a phosphatidylserine flippase in photoreceptor disc membranes. *J Biol*
996 *Chem* **284**:32670–32679. doi:10.1074/jbc.M109.047415
997 Coleman JA, Molday RS. 2011. Critical role of the beta-subunit CDC50A in the stable expression,
998 assembly, subcellular localization, and lipid transport activity of the P4-ATPase ATP8A2. *J Biol*
999 *Chem* **286**:17205–17216. doi:10.1074/jbc.M111.229419
1000 Danko S, Daiho T, Yamasaki K, Liu X, Suzuki H. 2009. Formation of the stable structural analog of
1001 ADP-sensitive phosphoenzyme of Ca2+-ATPase with occluded Ca2+ by beryllium fluoride: structural
1002 changes during phosphorylation and isomerization. *J Biol Chem* **284**:22722–22735.
1003 doi:10.1074/jbc.M109.029702
1004 Deng B-C, Lv S, Cui W, Zhao R, Lu X, Wu J, Liu P. 2012. Novel ATP8B1 mutation in an adult male
1005 with progressive familial intrahepatic cholestasis. *World J Gastroenterol* **18**:6504–6509.
1006 doi:10.3748/wjg.v18.i44.6504
1007 Dickson EJ, Hille B. 2019. Understanding phosphoinositides: rare, dynamic, and essential
1008 membrane phospholipids. *Biochem J* **476**:1–23. doi:10.1042/BCJ20180022
1009 Dixon PH, Sambrotta M, Chambers J, Taylor-Harris P, Syngelaki A, Nicolaides K, Knisely AS,
1010 Thompson RJ, Williamson C. 2017. An expanded role for heterozygous mutations of ABCB4,
1011 ABCB11, ATP8B1, ABCC2 and TJP2 in intrahepatic cholestasis of pregnancy. *Sci Rep* **7**:11823.
1012 doi:10.1038/s41598-017-11626-x
1013 Ekberg K, Palmgren MG, Veierskov B, Buch-Pedersen MJ. 2010. A novel mechanism of P-type
1014 ATPase autoinhibition involving both termini of the protein. *J Biol Chem* **285**:7344–7350.

1015 doi:10.1074/jbc.M109.096123
1016 Emsley P, Lohkamp B, Scott WG, Cowtan K. 2010. Features and development of Coot. *Acta*
1017 *Crystallogr D Biol Crystallogr* **66**:486–501. doi:10.1107/S0907444910007493
1018 Gantzel RH, Mogensen LS, Mikkelsen SA, Vilsen B, Molday RS, Vestergaard AL, Andersen JP.
1019 2017. Disease mutations reveal residues critical to the interaction of P4-ATPases with lipid
1020 substrates. *Sci Rep* **7**:10418. doi:10.1038/s41598-017-10741-z
1021 Gautherot J, Delautier D, Maubert M-A, Aït-Slimane T, Bolbach G, Delaunay J-L, Durand-Schneider
1022 A-M, Firrincieli D, Barbu V, Chignard N, Housset C, Maurice M, Falguières T. 2014. Phosphorylation
1023 of ABCB4 impacts its function: insights from disease-causing mutations. *Hepatol Baltim Md* **60**:610–
1024 621. doi:10.1002/hep.27170
1025 Hancock JF, Paterson H, Marshall CJ. 1990. A polybasic domain or palmitoylation is required in
1026 addition to the CAAX motif to localize p21ras to the plasma membrane. *Cell* **63**:133–139.
1027 doi:10.1016/0092-8674(90)90294-o
1028 Hanson PK, Malone L, Birchmore JL, Nichols JW. 2003. Lem3p is essential for the uptake and
1029 potency of alkylphosphocholine drugs, edelfosine and miltefosine. *J Biol Chem* **278**:36041–36050.
1030 doi:10.1074/jbc.M305263200
1031 Hiraizumi M, Yamashita K, Nishizawa T, Nureki O. 2019. Cryo-EM structures capture the transport
1032 cycle of the P4-ATPase flippase. *Science* **365**:1149–1155. doi:10.1126/science.aay3353
1033 Holemans T, Sørensen DM, van Veen S, Martin S, Hermans D, Kemmer GC, Van den Haute C,
1034 Baekelandt V, Günther Pomorski T, Agostinis P, Wuytack F, Palmgren M, Eggermont J, Vangheluwe
1035 P. 2015. A lipid switch unlocks Parkinson's disease-associated ATP13A2. *Proc Natl Acad Sci U S A*
1036 **112**:9040–9045. doi:10.1073/pnas.1508220112
1037 Huttlin EL, Jedrychowski MP, Elias JE, Goswami T, Rad R, Beausoleil SA, Villén J, Haas W, Sowa
1038 ME, Gygi SP. 2010. A tissue-specific atlas of mouse protein phosphorylation and expression. *Cell*
1039 **143**:1174–1189. doi:10.1016/j.cell.2010.12.001
1040 Jacquemin E. 2012. Progressive familial intrahepatic cholestasis. *Clin Res Hepatol Gastroenterol* **36**
1041 **Suppl 1**:S26-35. doi:10.1016/S2210-7401(12)70018-9
1042 Jacquot A, Montigny C, Hennrich H, Barry R, le Maire M, Jaxel C, Holthuis J, Champeil P, Lenoir G.
1043 2012. Phosphatidylserine stimulation of Drs2p·Cdc50p lipid translocase dephosphorylation is
1044 controlled by phosphatidylinositol-4-phosphate. *J Biol Chem* **287**:13249–13261.
1045 doi:10.1074/jbc.M111.313916
1046 Klodos I, Esmann M, Post RL. 2002. Large-scale preparation of sodium-potassium ATPase from
1047 kidney outer medulla. *Kidney Int* **62**:2097–2100. doi:10.1046/j.1523-1755.2002.00654.x
1048 Klomp LWJ, Vargas JC, van Mil SWC, Pawlikowska L, Strautnieks SS, van Eijk MJT, Juijn JA,
1049 Pabón-Peña C, Smith LB, DeYoung JA, Byrne JA, Gombert J, van der Brugge G, Berger R,

1050 Jankowska I, Pawlowska J, Villa E, Knisely AS, Thompson RJ, Freimer NB, Houwen RHJ, Bull LN.
1051 2004. Characterization of mutations in ATP8B1 associated with hereditary cholestasis. *Hepatol*
1052 *Baltim Md* **40**:27–38. doi:10.1002/hep.20285
1053 Kobayashi T, Menon AK. 2018. Transbilayer lipid asymmetry. *Curr Biol CB* **28**:R386–R391.
1054 doi:10.1016/j.cub.2018.01.007
1055 Lee S, Uchida Y, Wang J, Matsudaira T, Nakagawa T, Kishimoto T, Mukai K, Inaba T, Kobayashi T,
1056 Molday RS, Taguchi T, Arai H. 2015. Transport through recycling endosomes requires EHD1
1057 recruitment by a phosphatidylserine translocase. *EMBO J* **34**:669–688.
1058 doi:10.15252/embj.201489703
1059 Lemmon MA. 2008. Membrane recognition by phospholipid-binding domains. *Nat Rev Mol Cell Biol*
1060 **9**:99–111. doi:10.1038/nrm2328
1061 Lenoir G, Williamson P, Puts CF, Holthuis JCM. 2009. Cdc50p plays a vital role in the ATPase
1062 reaction cycle of the putative aminophospholipid transporter Drs2p. *J Biol Chem* **284**:17956–17967.
1063 doi:10.1074/jbc.M109.013722
1064 Leventis PA, Grinstein S. 2010. The distribution and function of phosphatidylserine in cellular
1065 membranes. *Annu Rev Biophys* **39**:407–427. doi:10.1146/annurev.biophys.093008.131234
1066 Li P, Wang K, Salustros N, Grønberg C, Gourdon P. 2021. Structure and transport mechanism of
1067 P5B-ATPases. *Nat Commun* **12**:3973. doi:10.1038/s41467-021-24148-y
1068 López-Marqués RL, Poulsen LR, Bailly A, Geisler M, Pomorski TG, Palmgren MG. 2015. Structure
1069 and mechanism of ATP-dependent phospholipid transporters. *Biochim Biophys Acta* **1850**:461–475.
1070 doi:10.1016/j.bbagen.2014.04.008
1071 Lyons JA, Timcenko M, Dieudonné T, Lenoir G, Nissen P. 2020. P4-ATPases: how an old dog learnt
1072 new tricks - structure and mechanism of lipid flippases. *Curr Opin Struct Biol* **63**:65–73.
1073 doi:10.1016/j.sbi.2020.04.001
1074 Marat AL, Haucke V. 2016. Phosphatidylinositol 3-phosphates-at the interface between cell
1075 signalling and membrane traffic. *EMBO J* **35**:561–579. doi:10.15252/embj.201593564
1076 Montigny C, Lyons J, Champeil P, Nissen P, Lenoir G. 2016. On the molecular mechanism of
1077 flippase- and scramblase-mediated phospholipid transport. *Biochim Biophys Acta* **1861**:767–783.
1078 doi:10.1016/j.bbalip.2015.12.020
1079 Mücksch F, Citir M, Lüchtenborg C, Glass B, Traynor-Kaplan A, Schultz C, Brügger B, Kräusslich H-
1080 G. 2019. Quantification of phosphoinositides reveals strong enrichment of PIP2 in HIV-1 compared
1081 to producer cell membranes. *Sci Rep* **9**:17661. doi:10.1038/s41598-019-53939-z
1082 Muñoz-Martínez F, Torres C, Castanys S, Gamarro F. 2010. CDC50A plays a key role in the uptake
1083 of the anticancer drug perifosine in human carcinoma cells. *Biochem Pharmacol* **80**:793–800.
1084 doi:10.1016/j.bcp.2010.05.017

1085 Murate M, Abe M, Kasahara K, Iwabuchi K, Umeda M, Kobayashi T. 2015. Transbilayer distribution
1086 of lipids at nano scale. *J Cell Sci* **128**:1627–1638. doi:10.1242/jcs.163105
1087 Naito T, Takatsu H, Miyano R, Takada N, Nakayama K, Shin H-W. 2015. Phospholipid Flippase
1088 ATP10A Translocates Phosphatidylcholine and Is Involved in Plasma Membrane Dynamics. *J Biol*
1089 *Chem* **290**:15004–15017. doi:10.1074/jbc.M115.655191
1090 Nakanishi H, Irie K, Segawa K, Hasegawa K, Fujiyoshi Y, Nagata S, Abe K. 2020a. Crystal structure
1091 of a human plasma membrane phospholipid flippase. *J Biol Chem* **295**:10180–10194.
1092 doi:10.1074/jbc.RA120.014144
1093 Nakanishi H, Nishizawa T, Segawa K, Nureki O, Fujiyoshi Y, Nagata S, Abe K. 2020b. Transport
1094 Cycle of Plasma Membrane Flippase ATP11C by Cryo-EM. *Cell Rep* **32**:108208.
1095 doi:10.1016/j.celrep.2020.108208
1096 Natarajan P, Liu K, Patil DV, Sciorra VA, Jackson CL, Graham TR. 2009. Regulation of a Golgi
1097 flippase by phosphoinositides and an ArfGEF. *Nat Cell Biol* **11**:1421–1426. doi:10.1038/ncb1989
1098 Noe J, Hagenbuch B, Meier PJ, St-Pierre MV. 2001. Characterization of the mouse bile salt export
1099 pump overexpressed in the baculovirus system. *Hepatology* **33**:1223–1231.
1100 doi:10.1053/jhep.2001.24171
1101 Onat OE, Gulsuner S, Bilguvar K, Nazli Basak A, Topaloglu H, Tan M, Tan U, Gunel M, Ozcelik T.
1102 2013. Missense mutation in the ATPase, aminophospholipid transporter protein ATP8A2 is
1103 associated with cerebellar atrophy and quadrupedal locomotion. *Eur J Hum Genet EJHG* **21**:281–
1104 285. doi:10.1038/ejhg.2012.170
1105 Painter JN, Savander M, Ropponen A, Nupponen N, Riikonen S, Ylikorkala O, Lehesjoki A-E,
1106 Aittomäki K. 2005. Sequence variation in the ATP8B1 gene and intrahepatic cholestasis of
1107 pregnancy. *Eur J Hum Genet EJHG* **13**:435–439. doi:10.1038/sj.ejhg.5201355
1108 Pettersen EF, Goddard TD, Huang CC, Meng EC, Couch GS, Croll TI, Morris JH, Ferrin TE. 2021.
1109 UCSF ChimeraX: Structure visualization for researchers, educators, and developers. *Protein Sci*
1110 *Publ Protein Soc* **30**:70–82. doi:10.1002/pro.3943
1111 Platre MP, Bayle V, Armengot L, Bareille J, Marquès-Bueno MDM, Creff A, Maneta-Peyret L, Fiche
1112 J-B, Nollmann M, Miège C, Moreau P, Martinière A, Jaillais Y. 2019. Developmental control of plant
1113 Rho GTPase nano-organization by the lipid phosphatidylserine. *Science* **364**:57–62.
1114 doi:10.1126/science.aav9959
1115 Pomorski T, Lombardi R, Riezman H, Devaux PF, van Meer G, Holthuis JCM. 2003. Drs2p-related
1116 P-type ATPases Dnf1p and Dnf2p are required for phospholipid translocation across the yeast
1117 plasma membrane and serve a role in endocytosis. *Mol Biol Cell* **14**:1240–1254.
1118 doi:10.1091/mbc.e02-08-0501
1119 Pomorski TG, Menon AK. 2016. Lipid somersaults: Uncovering the mechanisms of protein-mediated

lipid flipping. *Prog Lipid Res* **64**:69–84. doi:10.1016/j.plipres.2016.08.003

Post RL, Hegyvary C, Kume S. 1972. Activation by adenosine triphosphate in the phosphorylation kinetics of sodium and potassium ion transport adenosine triphosphatase. *J Biol Chem* **247**:6530–6540.

Poulsen LR, López-Marqués RL, McDowell SC, Okkeri J, Licht D, Schulz A, Pomorski T, Harper JF, Palmgren MG. 2008. The Arabidopsis P4-ATPase ALA3 localizes to the golgi and requires a beta-subunit to function in lipid translocation and secretory vesicle formation. *Plant Cell* **20**:658–676. doi:10.1105/tpc.107.054767

Punjani A, Rubinstein JL, Fleet DJ, Brubaker MA. 2017. cryoSPARC: algorithms for rapid unsupervised cryo-EM structure determination. *Nat Methods* **14**:290–296. doi:10.1038/nmeth.4169

Punjani A, Zhang H, Fleet DJ. 2020. Non-uniform refinement: adaptive regularization improves single-particle cryo-EM reconstruction. *Nat Methods* **17**:1214–1221. doi:10.1038/s41592-020-00990-8

Riekhof WR, Wu J, Gijón MA, Zarini S, Murphy RC, Voelker DR. 2007. Lysophosphatidylcholine metabolism in Saccharomyces cerevisiae: the role of P-type ATPases in transport and a broad specificity acyltransferase in acylation. *J Biol Chem* **282**:36853–36861. doi:10.1074/jbc.M706718200

Roland BP, Naito T, Best JT, Arnaiz-Yépez C, Takatsu H, Yu RJ, Shin H-W, Graham TR. 2019. Yeast and human P4-ATPases transport glycosphingolipids using conserved structural motifs. *J Biol Chem* **294**:1794–1806. doi:10.1074/jbc.RA118.005876

Saffioti NA, de Sautu M, Riesco AS, Ferreira-Gomes MS, Rossi JPFC, Mangialavori IC. 2021. Conformational changes during the reaction cycle of plasma membrane Ca2+-ATPase in the autoinhibited and activated states. *Biochem J* **478**:2019–2034. doi:10.1042/BCJ20210036

Saito K, Fujimura-Kamada K, Furuta N, Kato U, Umeda M, Tanaka K. 2004. Cdc50p, a protein required for polarized growth, associates with the Drs2p P-type ATPase implicated in phospholipid translocation in Saccharomyces cerevisiae. *Mol Biol Cell* **15**:3418–3432. doi:10.1091/mbc.e03-11-0829

Segawa K, Kikuchi A, Noji T, Sugiura Y, Hiraga K, Suzuki C, Haginoya K, Kobayashi Y, Matsunaga M, Ochiai Y, Yamada K, Nishimura T, Iwasawa S, Shoji W, Sugihara F, Nishino K, Kosako H, Ikawa M, Uchiyama Y, Suematsu M, Ishikita H, Kure S, Nagata S. 2021. A sublethal ATP11A mutation associated with neurological deterioration causes aberrant phosphatidylcholine flipping in plasma membranes. *J Clin Invest* **131**:148005. doi:10.1172/JCI148005

Segawa K, Kurata S, Nagata S. 2018. The CDC50A extracellular domain is required for forming a functional complex with and chaperoning phospholipid flippases to the plasma membrane. *J Biol Chem* **293**:2172–2182. doi:10.1074/jbc.RA117.000289

1155 Segawa K, Kurata S, Nagata S. 2016. Human Type IV P-type ATPases That Work as Plasma
1156 Membrane Phospholipid Flippases and Their Regulation by Caspase and Calcium. *J Biol Chem*
1157 **291**:762–772. doi:10.1074/jbc.M115.690727
1158 Takatsu H, Tanaka G, Segawa K, Suzuki J, Nagata S, Nakayama K, Shin H-W. 2014. Phospholipid
1159 flippase activities and substrate specificities of human type IV P-type ATPases localized to the
1160 plasma membrane. *J Biol Chem* **289**:33543–33556. doi:10.1074/jbc.M114.593012
1161 Terwilliger TC, Sobolev OV, Afonine PV, Adams PD. 2018. Automated map sharpening by
1162 maximization of detail and connectivity. *Acta Crystallogr Sect Struct Biol* **74**:545–559.
1163 doi:10.1107/S2059798318004655
1164 Timcenko M, Dieudonné T, Montigny C, Boesen T, Lyons JA, Lenoir G, Nissen P. 2021. Structural
1165 Basis of Substrate-Independent Phosphorylation in a P4-ATPase Lipid Flippase. *J Mol Biol* 167062.
1166 doi:10.1016/j.jmb.2021.167062
1167 Timcenko M, Lyons JA, Januliene D, Ulstrup JJ, Dieudonné T, Montigny C, Ash M-R, Karlsen JL,
1168 Boesen T, Kühlbrandt W, Lenoir G, Moeller A, Nissen P. 2019. Structure and autoregulation of a P4-
1169 ATPase lipid flippase. *Nature* **571**:366–370. doi:10.1038/s41586-019-1344-7
1170 Tomita A, Daiho T, Kusakizako T, Yamashita K, Ogasawara S, Murata T, Nishizawa T, Nureki O.
1171 2021. Cryo-EM reveals mechanistic insights into lipid-facilitated polyamine export by human
1172 ATP13A2. *Mol Cell* **81**:4799-4809.e5. doi:10.1016/j.molcel.2021.11.001
1173 Tsai P-C, Hsu J-W, Liu Y-W, Chen K-Y, Lee F-JS. 2013. Arl1p regulates spatial membrane
1174 organization at the trans-Golgi network through interaction with Arf-GEF Gea2p and flippase Drs2p.
1175 *Proc Natl Acad Sci U S A* **110**:E668-677. doi:10.1073/pnas.1221484110
1176 van der Mark VA, Elferink RPJO, Paulusma CC. 2013. P4 ATPases: flippases in health and disease.
1177 *Int J Mol Sci* **14**:7897–7922. doi:10.3390/ijms14047897
1178 van der Velden LM, Wichers CGK, van Breevoort AED, Coleman JA, Molday RS, Berger R, Klomp
1179 LWJ, van de Graaf SFJ. 2010. Heteromeric interactions required for abundance and subcellular
1180 localization of human CDC50 proteins and class 1 P4-ATPases. *J Biol Chem* **285**:40088–40096.
1181 doi:10.1074/jbc.M110.139006
1182 van Meer G. 2011. Dynamic transbilayer lipid asymmetry. *Cold Spring Harb Perspect Biol* **3**.
1183 doi:10.1101/cshperspect.a004671
1184 van Meer G, Voelker DR, Feigenson GW. 2008. Membrane lipids: where they are and how they
1185 behave. *Nat Rev Mol Cell Biol* **9**:112–124. doi:10.1038/nrm2330
1186 Verkleij AJ, Zwaal RF, Roelofsen B, Comfurius P, Kastelijn D, van Deenen LL. 1973. The asymmetric
1187 distribution of phospholipids in the human red cell membrane. A combined study using
1188 phospholipases and freeze-etch electron microscopy. *Biochim Biophys Acta* **323**:178–193.
1189 doi:10.1016/0005-2736(73)90143-0

1190 Vestergaard AL, Coleman JA, Lemmin T, Mikkelsen SA, Molday LL, Vilsen B, Molday RS, Dal Peraro
1191 M, Andersen JP. 2014. Critical roles of isoleucine-364 and adjacent residues in a hydrophobic gate
1192 control of phospholipid transport by the mammalian P4-ATPase ATP8A2. *Proc Natl Acad Sci U S A*
1193 **111**:E1334-1343. doi:10.1073/pnas.1321165111
1194 Villén J, Beausoleil SA, Gerber SA, Gygi SP. 2007. Large-scale phosphorylation analysis of mouse
1195 liver. *Proc Natl Acad Sci U S A* **104**:1488–1493. doi:10.1073/pnas.0609836104
1196 Wang J, Molday LL, Hii T, Coleman JA, Wen T, Andersen JP, Molday RS. 2018. Proteomic Analysis
1197 and Functional Characterization of P4-ATPase Phospholipid Flippases from Murine Tissues. *Sci*
1198 *Rep* **8**:10795. doi:10.1038/s41598-018-29108-z
1199 Yang J, Yan R, Roy A, Xu D, Poisson J, Zhang Y. 2015. The I-TASSER Suite: protein structure and
1200 function prediction. *Nat Methods* **12**:7–8. doi:10.1038/nmeth.3213
1201 Yeung T, Heit B, Dubuisson J-F, Fairn GD, Chiu B, Inman R, Kapus A, Swanson M, Grinstein S.
1202 2009. Contribution of phosphatidylserine to membrane surface charge and protein targeting during
1203 phagosome maturation. *J Cell Biol* **185**:917–928. doi:10.1083/jcb.200903020
1204 Zhou X, Sebastian TT, Graham TR. 2013. Auto-inhibition of Drs2p, a yeast phospholipid flippase, by
1205 its carboxyl-terminal tail. *J Biol Chem* **288**:31807–31815. doi:10.1074/jbc.M113.481986
1206
1207